DYNAMIC MODELLING IN MICROMACHINING

A THESIS SUBMITTED TO
THE GRADUATE SCHOOL OF NATURAL AND APPLIED SCIENCES
OF
MIDDLE EAST TECHNICAL UNIVERSITY

BY

EMRE ERSOY YILMAZ

IN PARTIAL FULFILLMENT OF THE REQUIREMENTS
FOR
THE DEGREE OF MASTER OF SCIENCE
IN
MECHANICAL ENGINEERING

DECEMBER 2015

Approval of the thesis:

DYANMIC MODELLING IN MICROMACHINING

Submitted by **EMRE ERSOY YILMAZ** in partial fulfillment of the requirements for the degree of **Master of Science in Mechanical Engineering Department, Middle East Technical University** by,

Prof. Dr. Gülbin Dural _____
Dean, Graduate School of **Natural and Applied Sciences**

Prof. Dr. Tuna Balkan _____
Head of Department, **Mechanical Engineering**

Prof. Dr. H. Nevzat Özgüven _____
Supervisor, **Mechanical Engineering Dept., METU**

Prof. Dr. Erhan Budak _____
Co-Supervisor, **Faculty of Engineering and Natural Sciences, SU**

Examining Committee Members:

Assoc. Prof. Dr. Yiğit Yazıcıoğlu _____
Mechanical Engineering Dept., METU

Prof. Dr. H. Nevzat Özgüven _____
Mechanical Engineering Dept., METU

Prof. Dr. Erhan Budak _____
Faculty of Engineering and Natural Sciences, SU

Assoc. Prof. Dr. Ender Ciğeroğlu _____
Mechanical Engineering Dept., METU

Assist. Prof. Dr. Gökhan O. Özgen _____
Mechanical Engineering Dept., METU

Date: 09.12.2015

I hereby declare that all information in this document has been obtained and presented in accordance with academic rules and ethical conduct. I also declare that, as required by these rules and conduct, I have fully cited and referenced all materials and results that are not original to this work.

Name, Last name : Emre Ersoy Yılmaz

Signature :

ABSTRACT

DYNAMIC MODELLING IN MICROMACHINING

Yılmaz, Emre Ersoy

M.S., Department of Mechanical Engineering

Supervisor: Prof. Dr. H. Nevzat Özgüven

Co-supervisor: Prof. Dr. Erhan Budak

December 2015, 63 pages

Micro milling applications are rapidly growing in various industries such as micro machines, medical, electro-mechanical component production etc. Due to very high precision requirements, dimensional accuracy and surface quality of micro milled components are very critical. As commonly known chatter vibrations arising due to instability in cutting yield poor surface finish and reduced tool life with potential damage to cutting edges and machine tool. Chatter vibrations are even more critical for micro milling tools due to their very flexible and weak bodies which may easily be damaged or broken under unstable chatter vibrations. Therefore, prediction of chatter stability limits is of utmost importance in order to achieve desired outcome in micro milling operations. The main problem in prediction of stability diagrams in micro milling has been the determination of micro mill frequency response function (FRF).

Measurement of FRF is usually performed using impact testing in conventional machining which is almost impossible in micromachining due to small tool size. In this thesis, analytical modeling for obtaining tool point FRF for micro end mills by using chatter tests is presented. First of all, Timoshenko beam model with gyroscopic effects is utilized to obtain point FRF at tool tip. Then, chatter detection in micro machining is investigated using three different sensors which are accelerometer, acoustic emission sensor and microphone. Next, chatter tests are performed with micro end mills and chatter frequencies are experimentally obtained. An inverse stability analysis is performed to obtain the modal parameters of the micro mill using the data obtained from chatter tests. These modal parameters are used to predict the stability diagram. Then, the predicted stability diagram is verified by using further chatter experiments. Afterwards, modal parameters are used to generate the point FRF of the micro end mill. This FRF is compared with the previously obtained theoretical FRF, and thus the theoretical model is updated to better represent the dynamics at the micro end mill which can be used to obtain stability diagram under different conditions. The results of this study will enable accurate prediction of the stability diagram for micro-milling operations and thus increase production rate.

ÖZ

MİKRO ÜRETİMDE DİNAMİK MODELLEME

Yılmaz, Emre Ersoy

Yüksek Lisans., Makina Mühendisliği Bölümü

Tez Yöneticisi: Prof. Dr. H. Nevzat Özgüven

Ortak Tez Yöneticisi: Prof. Dr. Erhan Budak

Aralık 2015, 63 sayfa

Medikal, elektronik, optik, savunma gibi çeşitli endüstrilerde mikro üretim uygulamaları hızla artmaktadır. Mikro üretimdeki yüksek hassasiyet gereksinimi dolayısıyla boyutsal isabetlilik ve yüzey kalitesi mikro üretimde kritiktir. Bilindiği gibi kesme sürecindeki kararsızlıktan kaynaklana tırlama titreşimleri kötü yüzey kalitesine yol açar ve kesici takıma zarar vererek ömrünün kısalmasına sebep olur. Mikro kesici takımlar normal takımlara kıyasla daha esnek ve zayıf bir yapıya sahip olduklarından tırlama titreşimleri mikro takımlar için daha da kritiktir. Tırlama titreşimleri gerçekleştiğinde mikro takımlar kolaylıkla hasar görebilir. Bu sebepten dolayı tırlama kararlılık limitlerinin tahmin edilmesi, üretim sürecinden istenen sonucun alınabilmesi için çok önemlidir. Kararlılık diyagramlarının belirlenmesindeki ana problem mikro

takımların uçlarındaki frekans tepki fonksiyonlarının (FTF) belirlenmesidir. Konvansiyonel takımlarda FTF'ler genellikle darbe testleri ile belirlenmektedir.Fakat, bu yöntemin, çok küçük olmalarından dolayı mikro takımlara uygulanması imkansızdır. Bu tezde, mikro takımların ucundaki FTF'yi analitik olarak belirleyen bir model sunulmuştur. İlk olarak takım ucundaki FTF, jiroskopik etkiler de dahil edilerek timoşenko kiriş modeli kullanılarak teorik olarak elde edilmiştir. Mikro üretimde tırlama tespiti için, ivmeölçer, akustik emisyon sensörü ve mikrofon olarak üç farklı sensor incelenmiştir. Daha sonra, mikro takım kullanılarak tırlama testleri gerçekleştirilmiştir ve deneysel tırlama frekansları elde edilmiştir. Tırlama testlerinden elde edilen verilerle, kararlılık analizi tersten uygulanarak mikro takımın modal parametreleri hesaplanmıştır. Bu modal parametreler kullanılarak bir kararlılık diyagramı elde edilmiştir. Elde edilen kararlılık diyagramı daha fazla tırlama testi yapılarak doğrulanmıştır. Hesaplanan modal parametreler ile mikro takımın FTF'si oluşturulmuştur. Bu FTF daha önce teorik olarak elde edilen FTF ile karşılaştırılarak teorik model güncellenmiştir. Böylelikle, farklı koşullar için kararlılık diyagramı çıkarmakta kullanılabilecek, takımın dinamiğini daha iyi temsil eden bir teorik model elde edilmiştir. Yapılan çalışma mikro frezelemede kararlılık diyagramlarının daha isabetli bulunmasını ve dolayısıyla üretim hızının artmasını sağlamıştır.

To My Family

ACKNOWLEDGEMENTS

First of all, I would like to thank my thesis advisor Prof. Dr. H. Nevzat Özgüven for sharing his knowledge and for his guidance during my graduate studies.

I also would like to thank Prof. Dr. Erhan Budak for his constant support and guidance throughout the study.

I would also like to express my gratitude to Dr. Orkun Özşahin for his help in programming. I also thank Hayri Bakioğlu, Ersen Hatipoğlu and Süleyman Tutkun for their help in the experiments.

This work is also supported by the graduate scholarship program, BİDEB-2210, of Scientific and Technological Research Council of Turkey (TUBITAK).

TABLE OF CONTENTS

LIST OF FIGURES

FIGURES

LIST OF TABLES

TABLES

CHAPTER 1

INTRODUCTION

In this introductory chapter the general knowledge about micromachining, chatter vibrations and the problems in prediction of chatter vibrations are presented.

1.1 Micro Machining and Chatter Stability

Micro milling has been an increasingly used method of production in various industries in recent years. Parts used in defense industry, medical and micro-electromechanical systems as well as jewelry are some of the examples where micro milling has been utilized. Micro milling processes are performed in machining centers which have position control in the order of microns and are capable of operating at high spindle speeds. These micro milling centers also have compact design compared to conventional machining centers as well as lower power consumption in order to have less thermal expansion in its structure during the operation. Structure of micro milling centers are also designed to have minimum impact from the changes of temperature so as to retain its positional precision. The machining tools used in micro milling also are compact in size due to the small size of the produced parts. Parts produced in micro milling are basically small in size and have high precision requirements. Micro milling process provides an efficient and economic means of production for low to medium amounts of such parts. There are several reasons for the increase in micro milling processes in the industry. First of all, due to advantages in energy, material and volume

consumption, there is a miniaturizing trend in many products. Moreover, micro milling can meet the required precision in a variety of applications.

Advances in medical science resulting in increased usage of small implants which in turn require micromachining is another reason for the increase in micro milling operations. Similarly, the advances in micro-electromechanical systems, which contain various miniature parts and require a method for a fast and low cost prototyping, is another cause for the increase in micro milling operations. All of these applications of micro milling require that the manufacturing process is stable. If the process is unstable a phenomenon called chatter vibrations occur during operation. This type of vibration manifests when the phase difference between the wavy surfaces left by each passing tooth become such that the maximum chip thickness start to exponentially grow while oscillating at a frequency close to a dominant structural mode of the system[1]. Although chatter occurs in conventional milling as well, the result of chatter is more severe in micro milling. In conventional milling chatter causes the efficiency to drop and decrease in the quality of the finished product, whereas in micro milling chatter can result in cutting tool breakage and scrap parts. Therefore, a stable cutting process is vital for micro milling operations. Usual practice in guaranteeing stable cutting process is by generating stability diagrams before operation and selecting the machining parameters according to these diagrams (Figure 1-1).

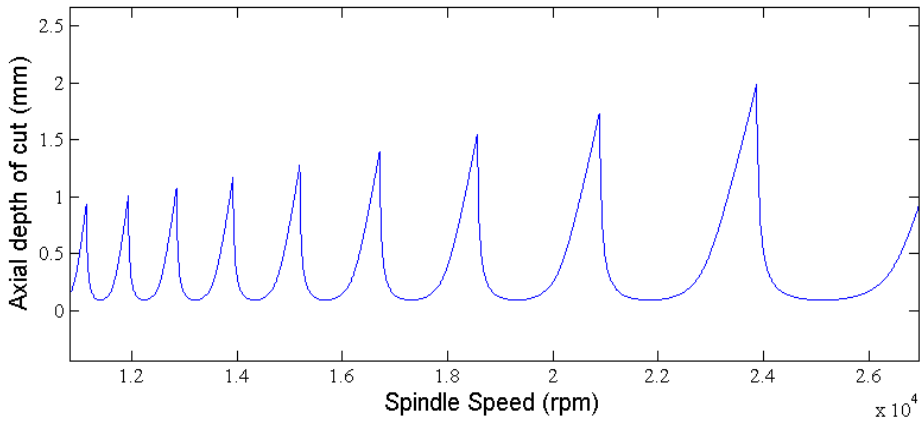

Figure 1-1: A Sample Stability Diagram

Once the stability diagram is generated, one can select a set of machining parameters from the region under the curve to guarantee a stable cutting operation. Generating such stability diagrams require information about the workpiece and the cutting tool. The tool point frequency response function (FRF) is one of the vital information required for obtaining stability diagrams. Developing a reliable approach for obtaining tool point FRFs for micro milling tools is the aim of this thesis.

1.2 Literature Review

Experimental modal analysis is the most common method of determining the tool point FRF [1]. However due to their fragile structures, impact testing is not suitable for micro milling tools. Cutting tool used in micro milling cannot be exited with impact hammer without damaging the tool. Therefore other methods are implemented in obtaining point FRFs of micro tools. The tool point FRF can be obtained without the experiments by modeling the parts of the structure using various beam models and then coupling these substructures to obtain the FRF of the complete structure [2-4]. Schmitz et al. [5-6] proposed the receptance coupling method to obtain tool point FRFs of non-rotating multi segmented beams. In the earlier works, beam segments are modelled as Euler-Bernoulli beams and the contact points between the substructures are modelled with linear stiffness and linear damping [7]. Park et al. [8] also considered rotary stiffness and damping in his work. Ertürk [9] modeled the segments of the structure with Timoshenko beam model while only considering linear stiffness and linear damping at the joints. While the fluted region of the cutting tool is modeled with an equivalent radius in previous works Filiz [10] further modeled the fluted region as a twisted beam to better represent its effect on the FRF. Kıvanç [11] calculated an equivalent radius for the fluted part by computing the second moment of its cross-sectional area.

Works on the micro milling stability are not very high in number. Chae et al. [12] compiled the research in micro-milling and suggested areas of research to improve micro-milling operations. Afazov et al. [13] implemented the stability models used in conventional machining to micromachining and researched the effects of cutting tool edge radius on the stability diagram. Mascardelli et al. [14] used receptance coupling

method to couple micro tool FRF obtained by finite element method with spindle-holder FRF measured with modal experiments. Rahnama et al. [15] worked on the cutting process dynamic. In his research, receptance coupling method is used to model the micro milling system and the stability analysis is performed considering the process damping effects. In later works Park [16] modelled the uncertainty during cutting process by considering the cutting parameters as variables changing within certain range instead of constants. Movahhedy et al. [17] further investigated the effect of process damping on chatter instability in the micro-milling operations. Jin et al. [18] measured the FRF at fragile tool tip with specially designed piezo-actuator which is capable of exciting without damaging the tool. In this research a dynamic model with velocity dependent process damping is presented and the model is verified with experiments. Afazov et al. [19] considered the process nonlinearities in the micro-milling such as nonlinearity of the uncut chip thickness and velocity dependent cutting forces in their research to model chatter in micro milling. Tajalli et al. [20] performed instability analysis of spinning micro-mill by semi-discretization considering the process damping effects. Bediz et al. [21] presented an experimental approach to obtain the dynamics of micro-milling tools. A custom made excitation system that is capable of exciting the system up to 20 kHz is utilized in their experiments. Aran [22] tried to obtain the tool point FRF by applying indirect modal analysis through an excitation force at a point on the tool shank.

1.3 Scope of Thesis

The main objective of the thesis is to research the dynamics of the tip of the micro milling tool. Tool point FRF of the micro mills is a crucial component in predicting stability limits of the machining process. Therefore, accurate determination of the tool FRF is very important. While the receptance coupling method is utilized to couple the FRFs of cutting tool, tool holder and spindle considering the damping and stiffness at the joints, the micro milling tool is the dominating component in the resulting FRF due to its small size compared to the rest of the structure. Therefore the effects of stiffness and damping at joints as well as the FRF of spindle are relatively small compared to conventional machining centers. Therefore in this work accurate identifications of

spindle and joints are not pursued and the research is focused on the micro milling tool. Improving the accuracy of the analytically obtained FRF of the micro milling tools, as well as predicting chatter stability limits better in micro milling are the main outcome of this thesis.

1.4 Outline of Thesis

Outline of the thesis is as follows:

In Chapter 2, the theory of the analytical model is presented. First the mathematical expressions of rotating Timoshenko beam are given. Then the receptance coupling method which is used to couple the FRFs of the segments is explained. Next the analytical model is verified with Finite Element Method and experimental modal analysis.

In Chapter 3, inverse stability analysis is presented. The mathematical theory regarding the inverse stability method are explained. The method is verified with a simulated experiment.

In Chapter 4, experimental studies about chatter detection is presented. The chatter experiments are explained and the inverse stability analysis, introduced in Chapter 3, is applied to chatter data. Modal parameters obtained from the inverse stability analysis are utilized to generate the stability diagram. Then the predicted stability diagram is checked by further chatter experiments. Finally the mathematical model used in expressing the tool point FRF is updated. Several parameters in the model are considered for the updates in the model.

In Chapter 5, a brief summary of the thesis is given and the conclusions of the research are discussed. Also possible future work related with the thesis topic are suggested.

CHAPTER 2

MATHEMATICAL MODELLING

2.1 Rotating Timoshenko Beam Model

In this section the Timoshenko beam model with gyroscopic effects will be presented. First, consider a beam element as shown in Figure 2-1. Here u_x and u_y are the lateral displacements whereas u_z represents the axial displacement. Similarly ϕ_x, ϕ_y and ϕ_z are the rotations in x, y and z axis, respectively.

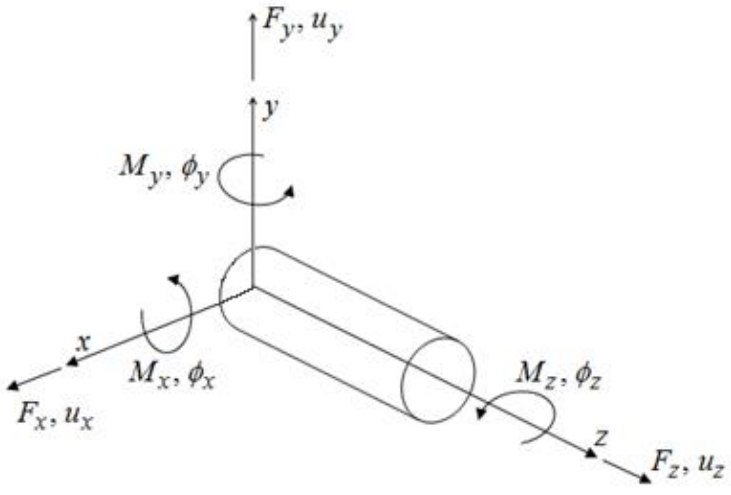

Figure 2-1: Beam Element of Rotating Timoshenko Beam Model

Equation of motion of such a beam element can be determined with Hamilton's principle as follows:

$$\delta \int_{t_1}^{t_2} (T - V + W) dt = 0 \tag{2.1}$$

In the equation (2.1) T, V, and W represent kinetic energy of the beam, potential energy of the beam and the work done by external forces and moments, respectively. The expressions for these terms are given as follows:

$$T = \int_0^L \frac{1}{2} \rho I \left(\left(\frac{\partial \phi_x}{\partial t} \right)^2 + \left(\frac{\partial \phi_y}{\partial t} \right)^2 \right) dz + \int_0^L \frac{1}{2} \rho A \left(\left(\frac{\partial u_x}{\partial t} \right)^2 + \left(\frac{\partial u_y}{\partial t} \right)^2 \right) dz +$$
$$\int_0^L \frac{1}{2} J \rho \Omega^2 dz + 2 \int_0^L \frac{1}{2} \rho I \Omega \left(\frac{\partial \phi_y}{\partial t} \right) dz \tag{2.2}$$

$$V = \int \frac{1}{2} E \varepsilon_{zz} dV + \int \frac{1}{2} kAG \gamma_{zx}^2 dV + \int \frac{1}{2} kAG \gamma_{yz}^2 dV \tag{2.3}$$

Where ρ is the density and A is the area of the cross section. I and J are area moment of inertia and polar moment of inertia about the neutral axis, respectively. Ω is the spinning speed of the beam. E and G are Young's modulus and shear modulus, respectively and k is the shear coefficient. Finally, ε term represents the normal strain and γ represents the shear strain.

In order to obtain the equation of motion strain-displacement relations are substituted into potential energy expression. Then the variations of the kinetic energy and potential energy expressions are substituted into equation (2.1) to obtain an expression for the equation of motion. This procedure results in four equations as shown below [23]:

$$\rho A \frac{\partial^2 u_x}{\partial t^2} - kAG \left(-\frac{\partial \phi_y}{\partial z} + \frac{\partial^2 u_x}{\partial z^2} \right) = 0 \tag{2.4}$$

$$\rho A \frac{\partial^2 u_y}{\partial t^2} - kAG \left(\frac{\partial \phi_x}{\partial z} + \frac{\partial^2 u_y}{\partial z^2} \right) = 0 \tag{2.5}$$

$$\rho I \frac{\partial^2 \phi_x}{\partial t^2} + 2\Omega I \rho \frac{\partial \phi_x}{\partial t} - EI \frac{\partial^2 \phi_x}{\partial z^2} + kAG \left(\phi_x + \frac{\partial u_y}{\partial z} \right) = 0 \tag{2.6}$$

$$\rho I \frac{\partial^2 \phi_y}{\partial t^2} - 2\Omega I \rho \frac{\partial \phi_x}{\partial t} - EI \frac{\partial^2 \phi_y}{\partial z^2} + kAG \left(\phi_y - \frac{\partial u_x}{\partial z} \right) = 0 \tag{2.7}$$

For free-free boundaries the boundary conditions can be expressed as follows:

$$M_x(0,t) = \left(EI\frac{\partial \phi_x}{\partial z}\right)_{z=0} = 0 \tag{2.8}$$

$$M_y(0,t) = \left(EI\frac{\partial \phi_y}{\partial z}\right)_{z=0} = 0 \tag{2.9}$$

$$M_x(L,t) = \left(EI\frac{\partial \phi_x}{\partial z}\right)_{z=L} = 0 \tag{2.10}$$

$$M_y(L,t) = \left(EI\frac{\partial \phi_y}{\partial z}\right)_{z=L} = 0 \tag{2.11}$$

$$S_x(0,t) = \left(kAG\left(\frac{\partial u_y}{\partial z} + \phi_x\right)\right)_{z=0} = 0 \tag{2.12}$$

$$S_y(0,t) = \left(kAG\left(\frac{\partial u_x}{\partial z} - \phi_y\right)\right)_{z=0} = 0 \tag{2.13}$$

$$S_x(L,t) = \left(kAG\left(\frac{\partial u_y}{\partial z} + \phi_x\right)\right)_{z=L} = 0 \tag{2.14}$$

$$S_y(L,t) = \left(kAG\left(\frac{\partial u_x}{\partial z} - \phi_y\right)\right)_{z=L} = 0 \tag{2.15}$$

Eliminating rotation terms in the equations (2.4) to (2.7) and then assuming harmonic solution and applying separation of variables will result in ordinary differential equation for backward motion as follows [23]:

$$EI\frac{d^4U_y^b}{dz^4} + \left[\left(\rho I + \frac{E\rho I}{kG}\right)\omega^2 - 2\rho I\Omega\omega\right]\frac{d^2U_y^b}{dz^2} + \left[\frac{\rho^2 I}{kG}\omega^4 - 2\frac{\rho^2 I}{kG}\Omega\omega^3 - \rho A\omega^2\right]U_y^b = 0 \tag{2.16}$$

The expression for the forward motion is similarly given as follows:

$$EI\frac{d^4U_y^f}{dz^4} + \left[\left(\rho I + \frac{E\rho I}{kG}\right)\omega^2 + 2\rho I\Omega\omega\right]\frac{d^2U_y^f}{dz^2} + \left[\frac{\rho^2 I}{kG}\omega^4 + 2\frac{\rho^2 I}{kG}\Omega\omega^3 - \rho A\omega^2\right]U_y^f = 0 \tag{2.17}$$

For free vibration, solution is performed for backward motion as proposed by Aristizabal-Ochoa [24] as follows:

$$\begin{vmatrix} D_{11} & D_{12} \\ D_{21} & D_{22} \end{vmatrix} = D_{11}D_{22} - D_{12}D_{21} = 0 \tag{2.18}$$

where;

$$D_{11} = (\alpha - \lambda)cos(\alpha L) + (\lambda - \alpha)cosh(\beta L) \tag{2.19}$$

$$D_{12} = (\lambda - \alpha)sin(\alpha L) + \frac{\lambda\alpha}{\delta\beta}(\beta - \delta)sinh(\beta L) \tag{2.20}$$

$$D_{21} = \delta\beta\,\frac{(\lambda-\alpha)}{\beta-\delta}sinh(\beta L) - \alpha\lambda sin(\alpha L) \tag{2.21}$$

$$D_{22} = \alpha\lambda\big(cosh(\beta L) - cos(\alpha L)\big) \tag{2.22}$$

$$\lambda = \frac{\alpha^2-K}{\alpha} \tag{2.23}$$

$$\delta = \frac{\beta^2+K}{\beta} \tag{2.24}$$

$$K = \frac{\rho A\omega^2}{kAG} \tag{2.25}$$

$$\alpha = \sqrt{\eta + \varepsilon} \tag{2.26}$$

$$\beta = \sqrt{-\eta + \varepsilon} \tag{2.27}$$

$$\eta = \frac{b}{2} \tag{2.28}$$

$$\varepsilon = \frac{\sqrt{b^2-4d}}{2} \tag{2.29}$$

$$b = \frac{\left[\left(\rho I + \frac{E\rho I}{kG}\right)\omega^2 - 2\rho I\Omega\omega\right]}{EI} \tag{2.30}$$

$$d = \frac{\left[\frac{\rho^2 I}{kG}\omega^4 - 2\frac{\rho^2 I}{kG}\Omega\omega^3 - \rho A\omega^2\right]}{EI} \tag{2.31}$$

Using the characteristic equation (2.18) the natural frequencies of each mode and the corresponding frequency numbers α_r and β_r can be calculated. Finally the eigenvectors corresponding to each mode can be expressed as follows:

$$U_y^b(z) = A_r(C_1 \sin(\alpha_r z) + C_2 \cos(\alpha_r z) + C_3 \sinh(\beta_r z) + C_4 \cosh(\beta_r z)) \quad (2.32)$$

$$\theta_x^b(z) = A_r[\lambda_r(C_1 \cos(\alpha_r z) - C_2 \sin(\alpha_r z))] + A_r[\delta_r(C_3 \cosh(\beta_r z) - C_4 \sin h(\beta_r z))] \quad (2.33)$$

where;

$$C_1 = C_1, \quad C_2 = -C_1 \frac{D_{11}}{D_{12}}, \quad C_3 = C_1 \frac{\alpha_r - \lambda_r}{\delta_r - \beta_r}, \quad C_4 = -C_1 \frac{\alpha_r \lambda_r D_{11}}{\delta_r \beta_r D_{12}} \quad (2.34)$$

The free vibration solution for the forward motion is similar. The only differences are on the terms expressed in equations (2.30) and (2.31). In the forward motion solution, the speed dependent terms in these expressions have opposite signs.

In order to obtain the forced response of a rotating Timoshenko beam with the excitation force located at $z=z_n$ in y direction, equations (2.4) to (2.7) can be expressed as follows [23]:

$$[M]\{\ddot{q}\} + [G]\{\dot{q}\} + [K]\{q\} = \{F(t)\} \quad (2.35)$$

where M, G, K, q and F(t) are expressed as follows:

$$[M] = \begin{bmatrix} \rho A & 0 & 0 & 0 \\ 0 & \rho I & 0 & 0 \\ 0 & 0 & \rho A & 0 \\ 0 & 0 & 0 & \rho I \end{bmatrix} \quad (2.36)$$

$$[G] = \begin{bmatrix} 0 & 0 & 0 & 0 \\ 0 & 0 & 0 & 2\rho I\Omega \\ 0 & 0 & 0 & 0 \\ 0 & -2\rho I\Omega & 0 & 0 \end{bmatrix} \quad (2.37)$$

$$[K] = \begin{bmatrix} -kAG\frac{\partial^2}{\partial z^2} & -kAG\frac{\partial}{\partial z} & 0 & 0 \\ kAG\frac{\partial}{\partial z} & kAG - EI\frac{\partial^2}{\partial z^2} & 0 & 0 \\ 0 & 0 & -kAG\frac{\partial^2}{\partial z^2} & kAG\frac{\partial}{\partial z} \\ 0 & 0 & kAG\frac{\partial}{\partial z} & kAG - EI\frac{\partial^2}{\partial z^2} \end{bmatrix} \tag{2.38}$$

$$\{q\} = \begin{Bmatrix} u_y \\ \Phi_x \\ u_x \\ \Phi_y \end{Bmatrix} \tag{2.39}$$

$$\{F(t)\} = \begin{Bmatrix} F_y(t)\delta(z - z_n) \\ 0 \\ 0 \\ 0 \end{Bmatrix} \tag{2.40}$$

Since the system is non-self adjoint, it is necessary to express the equation of motion in state space as follows [23]:

$$\begin{bmatrix} 0 & M \\ M & G \end{bmatrix}\{\dot{w}\} = \begin{bmatrix} M & 0 \\ 0 & -K \end{bmatrix}\{w\} + \{Q(t)\} \tag{2.41}$$

where;

$$\{w\} = \begin{Bmatrix} \dot{q} \\ q \end{Bmatrix} \tag{2.42}$$

$$\{Q(t)\} = \begin{Bmatrix} 0 \\ \{F(t)\} \end{Bmatrix} \tag{2.43}$$

Such a system will have right and left eigenvectors. For non-self adjoint systems, left eigenvectors and complex conjugate of right eigenvectors are related with a constant which is a pure imaginary number. Also, for non-self adjoint systems left and right eigenvectors are biorthonormal. Forced response of the system is given as follows [23]:

$$u_y(z,t) = \sum_{l=b,f}\sum_{r=-\infty}^{\infty}\frac{U_{y_r}^l(z)^a\bar{U}_{y_r}^l(z=z_n)^aF_y(t)}{i\omega-\lambda_r^l}$$

$$= \sum_{l=b,f}\sum_{r=0}^{\infty}\left(\frac{U_{y_r}^l(z)^a\bar{U}_{y_r}^l(z_n)^aF_y(t)}{i\omega-\lambda_r^l} + \frac{\bar{U}_{y_r}^l(z)^a\bar{U}_{y_r}^l(z_n)^aF_y(t)}{i\omega-\bar{\lambda}_r^l}\right)$$

$$= \sum_{l=b,f} \sum_{r=0}^{\infty} \left(2i\omega_r \frac{U_{yr}^{l}(z)^{a} \bar{U}_{yr}^{l}(z=z_n)^{a} F_y(t)}{-\omega^2 - \left(\omega_r^{l}\right)^2} \right) \tag{2.44}$$

The receptance functions of the beam in y-z plane can be expressed as follows:

$$H_{iy,jy} = \frac{(u_y)^j}{F_y^i},\ N_{iy,jx} = \frac{(\phi_x)^j}{F_y^i},\ L_{ix,jy} = \frac{(u_y)^j}{M_x^i},\ P_{ix,jx} = \frac{(\phi_x)^j}{M_x^i} \tag{2.45}$$

Including the structural damping terms in the denominator of equation (2.44) and taking the rigid body terms outside the summation sign, the point and cross receptance functions in y-z plane can be obtained as follows [23]:

$$H_{iy,jy}(\omega) = -\frac{1}{\rho A L \omega^2} + \sum_{l=b,f} \sum_{r=1}^{\infty} \left(2i\omega_r{}^{l} \frac{U_{yr}^{l}(z_j) U_{yr}^{l}(z_i)}{-\omega^2 + \left(\omega_r^{l}\right)^2 (1+i\gamma)} \right) \tag{2.46}$$

$$N_{iy,jx}(\omega) = \sum_{l=b,f} \sum_{r=1}^{\infty} \left(2i\omega_r{}^{l} \frac{\theta_{xr}^{l}(z_j) U_{yr}^{l}(z_i)}{-\omega^2 + \left(\omega_r^{l}\right)^2 (1+i\gamma)} \right) \tag{2.47}$$

$$L_{ix,jy}(\omega) = \sum_{l=b,f} \sum_{r=1}^{\infty} \left(2i\omega_r{}^{l} \frac{U_{yr}^{l}(z_j) \theta_{xr}^{l}(z_i)}{-\omega^2 + \left(\omega_r^{l}\right)^2 (1+i\gamma)} \right) \tag{2.48}$$

$$P_{ix,jx}(\omega) = \sum_{l=b,f} \sum_{r=1}^{\infty} \left(2i\omega_r{}^{l} \frac{\theta_{xr}^{l}(z_j) \theta_{xr}^{l}(z_i)}{-\omega^2 + \left(\omega_r^{l}\right)^2 (1+i\gamma)} \right) \tag{2.49}$$

Because of the gyroscopic effects the cross FRFs between orthogonal planes are coupled and these cross FRFs can be expressed as follows [23]:

$$H_{ix,jy}(\omega) = \sum_{r=0}^{\infty} \left(2\omega \frac{U_{yr}^{b}(z_j) U_{yr}^{b}(z_i)}{-\omega^2 + \left(\omega_r^{b}\right)^2 (1+i\gamma)} \right) + \sum_{r=0}^{\infty} \left(-2\omega \frac{U_{yr}^{f}(z_j) U_{yr}^{f}(z_i)}{-\omega^2 + \left(\omega_r^{f}\right)^2 (1+i\gamma)} \right) \tag{2.50}$$

$$N_{iy,jy}(\omega) = \sum_{r=0}^{\infty} \left(2\omega \frac{\theta_{xr}^{b}(z_j) U_{yr}^{b}(z_i)}{-\omega^2 + \left(\omega_r^{b}\right)^2 (1+i\gamma)} \right) + \sum_{r=0}^{\infty} \left(-2\omega \frac{\theta_{xr}^{f}(z_j) U_{yr}^{f}(z_i)}{-\omega^2 + \left(\omega_r^{f}\right)^2 (1+i\gamma)} \right) \tag{2.51}$$

$$L_{ix,jx}(\omega) = \sum_{r=0}^{\infty} \left(-2\omega \frac{U_{yr}^{b}(z_j) \theta_{xr}^{b}(z_i)}{-\omega^2 + \left(\omega_r^{b}\right)^2 (1+i\gamma)} \right) + \sum_{r=0}^{\infty} \left(2\omega \frac{U_{yr}^{f}(z_j) \theta_{xr}^{f}(z_i)}{-\omega^2 + \left(\omega_r^{f}\right)^2 (1+i\gamma)} \right) \tag{2.52}$$

$$P_{ix,jy}(\omega) = \sum_{r=0}^{\infty} \left(2\omega \frac{\theta_{xr}^{b}(z_j) \theta_{xr}^{b}(z_i)}{-\omega^2 + \left(\omega_r^{b}\right)^2 (1+i\gamma)} \right) + \sum_{r=0}^{\infty} \left(-2\omega \frac{\theta_{xr}^{f}(z_j) \theta_{xr}^{f}(z_i)}{-\omega^2 + \left(\omega_r^{f}\right)^2 (1+i\gamma)} \right) \tag{2.53}$$

2.2 FRF's of Multi Segment Beams by Receptance Coupling

In this thesis the tool point FRF of a multi segment beam is calculated by using receptance coupling method. The method is represented graphically in Figure 2-2.

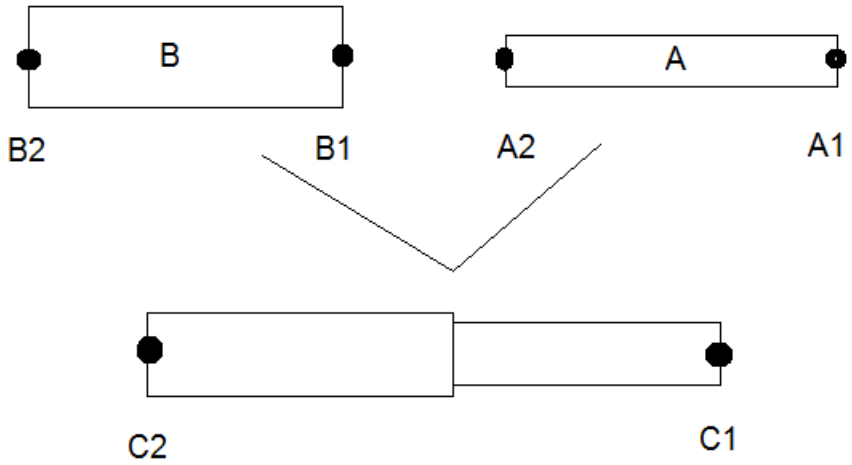

Figure 2-2: Receptance Coupling of Two Beams

Receptance coupling method uses FRF values at points A1, A2 of beam A and points B1, B2 of beam B in order to determine the FRFs at the tip points C1, C2 of the combined structure C. Receptance matrix for rotating Timoshenko beam at point A1 for an excitation applied at the same point can be defined as follows:

$$\begin{Bmatrix} u_{A1x} \\ \theta_{A1y} \\ u_{A1y} \\ \theta_{A1x} \end{Bmatrix} = \begin{bmatrix} H_{A1x,A1x} & L_{A1y,A1x} & H_{A1y,A1x} & L_{A1x,A1x} \\ N_{A1x,A1y} & P_{A1y,A1y} & N_{A1y,A1y} & P_{A1x,A1y} \\ H_{A1x,A1y} & L_{A1y,A1y} & H_{A1y,A1y} & L_{A1x,A1y} \\ N_{A1x,A1x} & P_{A1y,A1x} & N_{A1y,A1x} & P_{A1x,A1x} \end{bmatrix} \begin{Bmatrix} f_{A1x} \\ M_{A1y} \\ f_{A1y} \\ M_{A1x} \end{Bmatrix} \tag{2.54}$$

Here, the subscripts represent the location and direction of response and excitation. To clarify, in the term $P_{A1y,A1x}$ the first subscript A1y tells that the response is considered at A1 in the y direction while the second subscript tells that the excitation is applied at

A1 in x direction. The receptance matrix for the segment A can then be expressed as follows:

$$[A] = \begin{bmatrix} [A_{11}] & [A_{12}] \\ [A_{21}] & [A_{22}] \end{bmatrix} \tag{2.55}$$

where;

$$[A_{11}] = \begin{bmatrix} H_{A1x,A1x} & L_{A1y,A1x} & H_{A1y,A1x} & L_{A1x,A1x} \\ N_{A1x,A1y} & P_{A1y,A1y} & N_{A1y,A1y} & P_{A1x,A1y} \\ H_{A1x,A1y} & L_{A1y,A1y} & H_{A1y,A1y} & L_{A1x,A1y} \\ N_{A1x,A1x} & P_{A1y,A1x} & N_{A1y,A1x} & P_{A1x,A1x} \end{bmatrix} \tag{2.56}$$

$$[A_{12}] = \begin{bmatrix} H_{A1x,A2x} & L_{A1y,A2x} & H_{A1y,A2x} & L_{A1x,A2x} \\ N_{A1x,A2y} & P_{A1y,A2y} & N_{A1y,A2y} & P_{A1x,A2y} \\ H_{A1x,A2y} & L_{A1y,A2y} & H_{A1y,A2y} & L_{A1x,A2y} \\ N_{A1x,A2x} & P_{A1y,A2x} & N_{A1y,A2x} & P_{A1x,A2x} \end{bmatrix} \tag{2.57}$$

$$[A_{21}] = \begin{bmatrix} H_{A2x,A1x} & L_{A2y,A1x} & H_{A2y,A1x} & L_{A2x,A1x} \\ N_{A2x,A1y} & P_{A2y,A1y} & N_{A2y,A1y} & P_{A2x,A1y} \\ H_{A2x,A1y} & L_{A2y,A1y} & H_{A2y,A1y} & L_{A2x,A1y} \\ N_{A2x,A1x} & P_{A2y,A1x} & N_{A2y,A1x} & P_{A2x,A1x} \end{bmatrix} \tag{2.58}$$

$$[A_{22}] = \begin{bmatrix} H_{A2x,A2x} & L_{A2y,A2x} & H_{A2y,A2x} & L_{A2x,A2x} \\ N_{A2x,A2y} & P_{A2y,A2y} & N_{A2y,A2y} & P_{A2x,A2y} \\ H_{A2x,A2y} & L_{A2y,A2y} & H_{A2y,A2y} & L_{A2x,A2y} \\ N_{A2x,A2x} & P_{A2y,A2x} & N_{A2y,A2x} & P_{A2x,A2x} \end{bmatrix} \tag{2.59}$$

For segment B the FRF expressions are exactly the same. Making use of the continuity and the compatibility conditions at the connection point between segments A and B, the receptance coupling method yields the following expressions for the FRFs of the combined structure C [23]:

$$[C_{11}] = [A_{11}] - [A_{12}]\left[[A_{22}] + [B_{11}]\right]^{-1}[A_{21}] \tag{2.60}$$

$$[C_{12}] = [A_{12}]\left[[A_{22}] + [B_{11}]\right]^{-1}[B_{12}] \tag{2.61}$$

$$[C_{21}] = [B_{21}]\left[[A_{22}] + [B_{11}]\right]^{-1}[A_{21}] \tag{2.62}$$

$$[C_{22}] = [B_{22}] - [B_{12}]\left[[A_{22}] + [B_{11}]\right]^{-1}[B_{12}] \tag{2.63}$$

Equations (2.60)-(2.63) can be used to couple the FRFs of segments with different radii which are substructures of the same structure. To couple different structures (spindle, tool holder, cutting tool) which are connected by a joint, it is necessary to consider the joint dynamics as well.

To couple the FRFs of tool holder (H) and the cutting tool (T), the following expressions can be used [23].

$$[HT_{11}] = [T_{11}] - [T_{12}]\left[[T_{22}] + [K_{ht}]^{-1} + [H_{11}]\right]^{-1}[T_{21}] \tag{2.64}$$

$$[HT_{12}] = [T_{12}]\left[[T_{22}] + [K_{ht}]^{-1} + [H_{11}]\right]^{-1}[H_{21}] \tag{2.65}$$

$$[HT_{21}] = [H_{12}]\left[[T_{22}] + [K_{ht}]^{-1} + [H_{11}]\right]^{-1}[T_{21}] \tag{2.66}$$

$$[HT_{22}] = [H_{22}] - [H_{12}]\left[[T_{22}] + [K_{ht}]^{-1} + [H_{11}]\right]^{-1}[H_{12}] \tag{2.67}$$

where [HT] represents tool holder-cutting tool assembly and $[K_{ht}]$ is the complex stiffness matrix at the joint which can be expressed as follows [23]:

$$[K_{ht}] = \begin{bmatrix} k_x^{ht} + i\omega c_x^{ht} & 0 & 0 & 0 \\ 0 & k_{\theta_y}^{ht} + i\omega c_{\theta_y}^{ht} & 0 & 0 \\ 0 & 0 & k_y^{ht} + i\omega c_y^{ht} & 0 \\ 0 & 0 & 0 & k_{\theta_x}^{ht} + i\omega c_{\theta_x}^{ht} \end{bmatrix} \tag{2.68}$$

2.3 Verification of the Analytical Model

The analytical model for obtaining tool point FRF is verified using finite element method. ANSYS 14 software is used to obtain the FRF of a simple structure which is a 20 mm thick steel rod connected rigidly at its base. The rod has a length of 250 mm outside where it is grounded. The same structure is also modeled with analytical method. In order to represent a rigid connection; a large spindle size, a large holder size and high joint stiffness values at holder-tool joint is entered into the code. Resulting FRFs are given in the Figure 2-3.

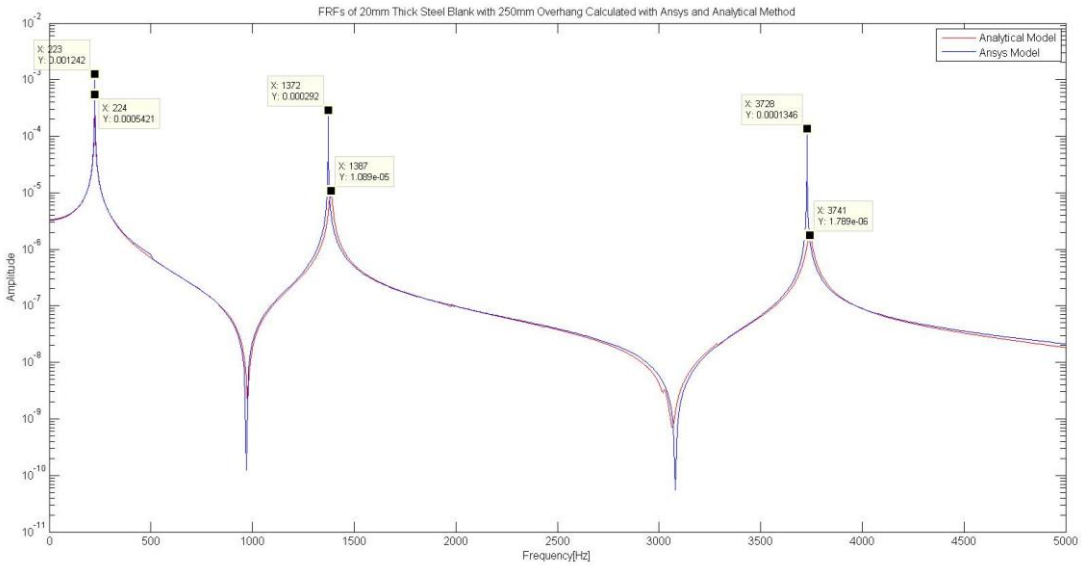

Figure 2-3: Analytical Model vs. FEM

In Figure 2-3, it can be seen that, FRF, obtained by analytical model are in agreement with those obtained from the finite element method. The amplitudes at second and third mode are slightly different and there are minor errors in the natural frequencies. However, the differences between the two FRFs are small and there are several possible causes for such errors. First of all, the accuracy of the finite element method depends on the mesh sizes used during the analysis. Higher amount of nodes improves accuracy but also increases the computation time. Second possible cause is the assumptions made in the code of ANSYS, especially the way of handling structural damping, which are not known. This may result in differences between the two FRFs and would explain the differences in the amplitudes. In order to further verify the analytical model, several impact tests are performed at different overhang lengths with a carbide blank. The experimental setup is shown in Figure 2-4.

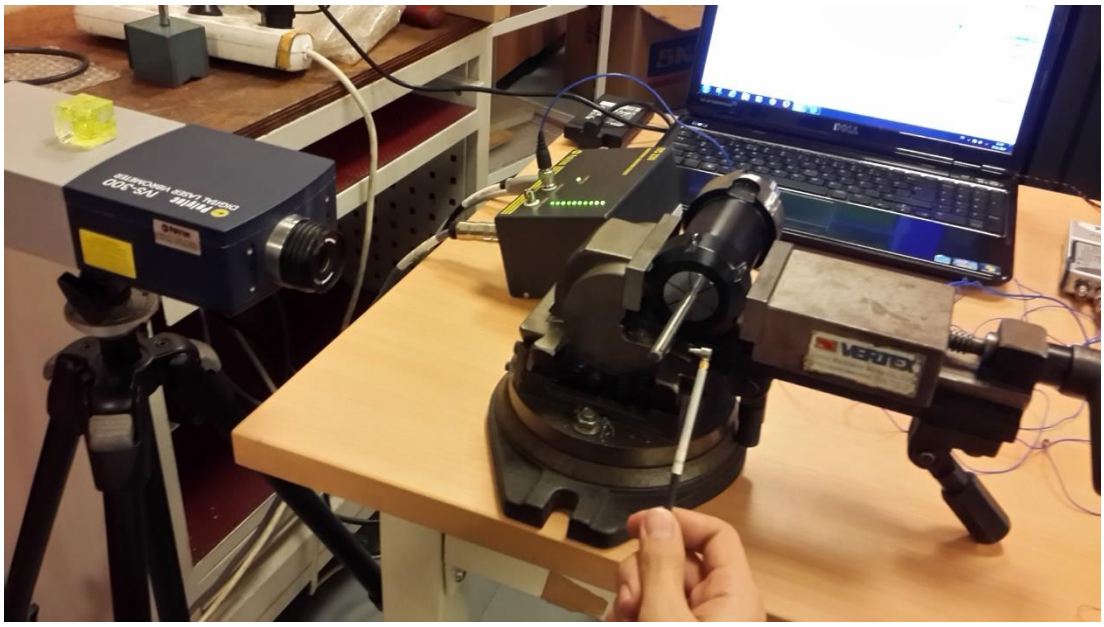

Figure 2-4: Impact Test Setup

The carbide blank is fastened to a tool holder which is fixed as rigidly as possible to a heavy clamp. The aim is to obtain the most rigid connection possible with a large base structure so that dynamics of the tool would dominate the tip FRF. Since the theoretical model requires a spindle, a tool holder and a tool measurements; the clamp part of the setup needs to be modelled as a spindle. This problem is tackled by selecting large values for spindle measurements in the theoretical model. Since the large base of the experimental setup and the large spindle will have little effect on the tip FRF, the error caused by this problem will be very small. The experimentally obtained and the analytically calculated FRFs are shown in Figure 2-5.

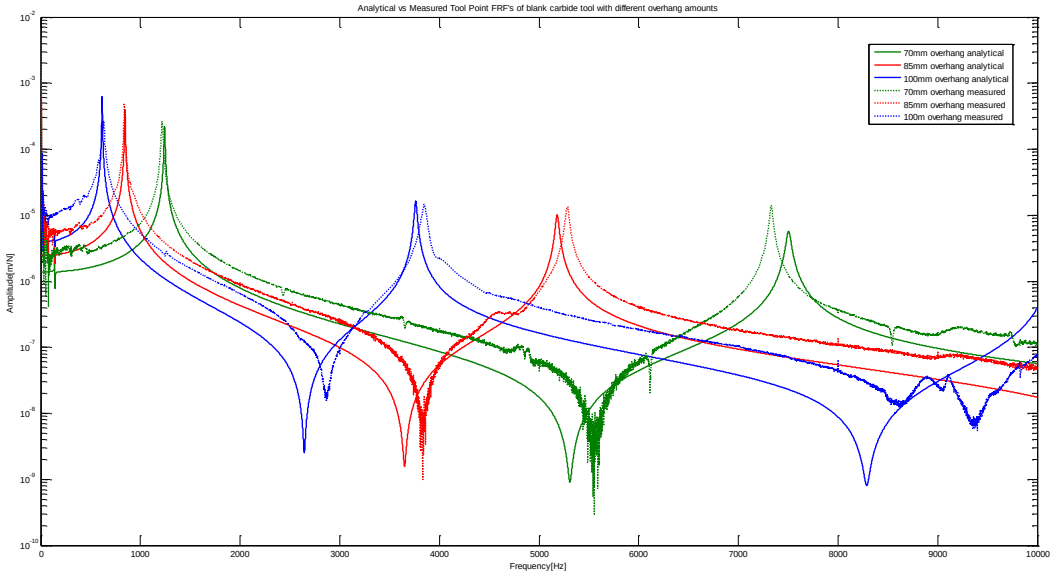

Figure 2-5: Experimental FRF vs. Analytical FRF for Different Overhang Lengths

The experimental and theoretical FRFs show peaks at nearly the same frequency in the first mode for all three cases. Although the trends of the curves are very similar, some differences in the resonance frequencies can be clearly seen in the second and following modes. Similarly, at very low frequencies there are considerable discrepancies between the FRFs. The error in the lower frequency is mainly caused by the low coherence value at these frequencies. In other words, the impact applied during the experiment failed to excite the system at these frequencies. Therefore, experimental FRF at very low frequencies are unreliable. The differences in the higher frequencies on the other hand, may be the result of errors in modelling the joint dynamics. Another impact test is performed utilizing a bigger clamping structure. The experimental setup is shown in Figure 2-6.

Figure 2-6: Experimental Setup of the 2nd Impact Test

The measured tip FRF and the theoretically obtained FRF are given in Figure 2-7.

Similar to the first impact test, the first modes of the FRFs show little difference and the error increases as the frequency increases. Again, the very low frequencies have low coherence and therefore the experimental FRFs at these frequencies are unreliable. The modes after the first resonance have some error; however, the first mode which has the highest amplitude is the most important one. Since the first mode is predicted very accurately in both experiments, it is reasonable to consider that the theoretical model is valid at this point.

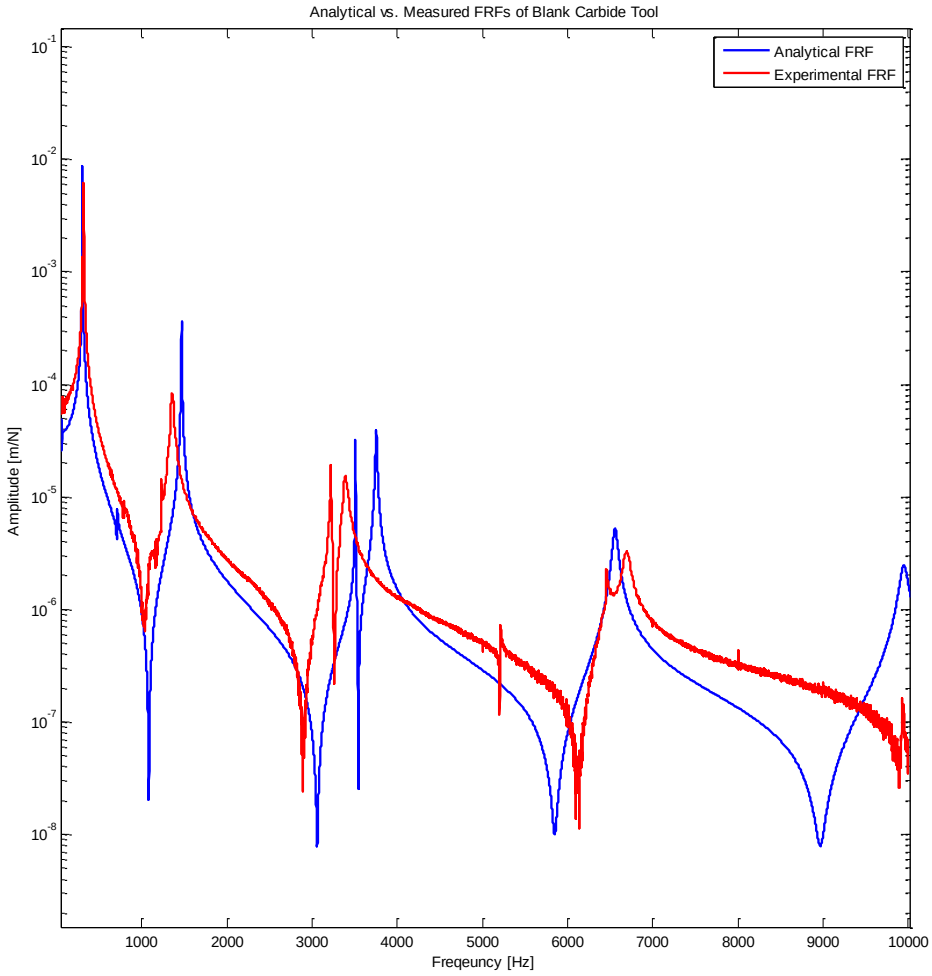

Figure 2-7: Experimental FRF vs. Analytical FRF for the 2nd Impact Test

CHAPTER 3

INVERSE STABILITY ANALYSIS

3.1 Inverse Stability Theory

As proposed by Budak and Altintaş, axial depth of cut and chatter frequency can be calculated as follows [25];

$$a_{\lim} = -\frac{2\pi \Lambda_R}{NK_t}(1+\kappa^2) \tag{3.1}$$

$$\omega_c T = \cos^{-1}\left(\frac{\kappa^2-1}{\kappa^2+1}\right) \tag{3.2}$$

where

$$\Lambda = (\Lambda_R + \Lambda_I i) = -\frac{1}{2a_0}\left(a_1 \pm \sqrt{{a_1}^2 - 4a_0}\right) \tag{3.3}$$

$$a_0 = G_{xx}G_{yy}\left(a_{xx}a_{yy} - a_{xy}a_{yx}\right) \tag{3.4}$$

$$a_1 = a_{xx}G_{xx} + a_{yy}G_{yy} \tag{3.5}$$

$$a_{xx} = \frac{1}{2}[\cos 2\phi - 2r\phi + r\sin 2\phi]_{\phi_{st}}^{\phi_{ex}} \tag{3.6}$$

$$a_{xy} = \frac{1}{2}[-\sin 2\phi - \phi + r\cos 2\phi]_{\phi_{st}}^{\phi_{ex}} \tag{3.7}$$

$$a_{yx} = \frac{1}{2}[-\sin 2\phi + 2\phi + r\cos 2\phi]_{\phi_{st}}^{\phi_{ex}} \tag{3.8}$$

$$a_{yy} = \frac{1}{2}[-\cos 2\phi - 2r\phi - r\sin 2\phi]_{\phi_{st}}^{\phi_{ex}} \tag{3.9}$$

$$\kappa = \frac{\Lambda_I}{\Lambda_R} \tag{3.10}$$

Here, G_{xx} and G_{yy} are the tool point FRFs in x and y directions, respectively, N is the number of cutting teeth, K_t is the tangential cutting force coefficient, r is the ratio of radial and tangential cutting force coefficients, ϕ_{st} and ϕ_{ex} are the start and exit angles of the cutting tooth, T is the tooth period.

$$G_{xx} = \sum_{j=1}^{n} \frac{A_j}{\omega_j{}^2 - \omega^2 + i2\xi_j\omega\omega_j} \tag{3.11}$$

Here, ξ_j is the damping ratio of the jth mode in x direction, ω_j is the natural frequency of the jth mode in x direction, A_j is the modal constant of the jth mode in x direction and ω is the excitation frequency.

Tool point FRF can be identified by equating the experimentally obtained chatter frequency and corresponding axial depth with analytical definitions of chatter frequency and corresponding axial depth of cut.

$$a_{lim}^{analytical} = a_{lim}^{experimental} \tag{3.12}$$

$$\omega_c^{analytical} = \omega_c^{experimental} \tag{3.13}$$

For each mode in the two orthogonal planes there exist 3 unknowns which are modal constant, natural frequency and damping ratio. However, equating experimentally and analytically obtained chatter frequencies and axial depths of cut yields only 2 equations. On the other hand it is possible to reduce the number of unknowns by considering the characteristics of stability theory. It is well known that different regions of the stability diagram are determined by different modes. Thus, instead of using summation term in the tool point FRF expression, each mode can be identified using different regions of stability diagram. Doing so would reduce the total number of unknowns to 6. The number of unknowns can be further reduced by recognizing that in micro-milling tool point FRFs in x and y directions are considered the same. Therefore, 2 equations with 3 unknowns can be obtained. It is not possible to solve for the 3 unknowns with only 2 equations. In order to solve this problem, the number of equations will be increased by performing more experiments. This point will be clarified after the final form of the mathematical expression is derived.

Rearranging equations (3.1) and (3.10) it is possible express Λ_R and Λ_I as follows:

$$\Lambda_R = -\frac{a_{lim} N K_t}{2\pi(1+\kappa^2)} \tag{3.14}$$

$$\Lambda_I = \kappa \Lambda_R \tag{3.15}$$

Substituting equations (3.4), (3.5), (3.14) and (3.15) into equation (3.3) would yield the following expression:

$$\frac{a_{lim} N K_t}{2\pi(1+\kappa^2)}(1 + i\kappa) = \frac{1}{2\alpha G_{xx}^2}\left(\beta G_{xx} \pm \sqrt{\beta^2 G_{xx}^2 - 4\alpha G_{xx}^2}\right) \tag{3.16}$$

where

$$\alpha = a_{xx}a_{yy} - a_{xy}a_{yx} \tag{3.17}$$

$$\beta = a_{xx} + a_{yy} \tag{3.18}$$

The only unknown in equation (3.16) is G_{xx}. Substituting equation (3.11) into equation (3.16) would yield:

$$\frac{\alpha a_{lim} N K_t}{\pi(1+\kappa^2)}(1 + i\kappa) = \frac{\beta\left(\frac{A_j}{{\omega_j}^2 - \omega^2 + i2\xi_j\omega\omega_j}\right) \pm \sqrt{(\beta^2 - 4\alpha)\left(\frac{A_j}{{\omega_j}^2 - \omega^2 + i2\xi_j\omega\omega_j}\right)^2}}{\left(\frac{A_j}{{\omega_j}^2 - \omega^2 + i2\xi_j\omega\omega_j}\right)^2} \tag{3.19}$$

Equation (3.19) is a complex equation with 3 unknowns which are ω_j, ξ_j and A_j. Since equation (3.19) will be evaluated at chatter frequency, the frequency term ω can be replaced with ω_c. In order to obtain the values of a_{lim} and ω_c experiments are required. As long as we use the same tool with the same overhang length in experiments, the FRF of the tool would remain the same. Therefore; performing experiments at different depths of cut and spindle speeds would increase the number of equations without increasing the number of unknowns. Experimenting twice is enough as it would yield 2 complex equations with 3 unknowns. Since two complex equations will provide four real equations, it is finally possible to solve for the 3 unknown modal parameters. Moreover, it is possible to further increase the number of equations, without increasing the number of unknowns, simply by performing more experiments.

3.2 Calculation of Modal Parameters Using Least Squares Regression

Applying inverse stability theory to data obtained from chatter tests would result in three parameters which are natural frequency, damping ratio and modal constant. To solve for three unknowns at least 3 equations are required. For each chatter test 2 equations can be obtained. Therefore at least 2 chatters tests are required to obtain the minimum necessary amount of equations. However; by increasing the number of tests, it is possible to increase the number of equations arbitrarily. When there are more equations than unknowns it is possible to use least squares method. Least squares method obtains a solution which minimizes the sum of the squares of errors in each equation. In the next chapter this procedure is utilized to solve for the modal parameters.

3.3 Verification of the Inverse Stability Analysis

Before applying the inverse stability theorem to real experimental data, it is first verified with a simulation. For a given FRF with known modal parameters a stability diagram is generated using CutPro software. On the generated stability curve 9 points are selected. Using the spindle speed, depth of cut and chatter frequency values of these 9 points inverse stability analysis is performed. The data of the selected points are given in Table 3-1. If the inverse stability method is applicable, the procedure is expected to give the modal parameters of the original FRF. The original and the generated FRFs are shown in Figure 3-1. The modal parameters are given Table 3-2.

Table 3-1: Selected Chatter Data for Verification

	Spindle Speed [rpm]	Depth of Cut [mm]	Chatter Frequency [Hz]
1st Point	3,755	2.677	478.08
2nd Point	3,795	2.509	479.37
3rd Point	3,815	2.358	480.62
4th Point	3,850	2.130	482.73

5th Point	3,895	1.894	485.3
6th Point	3,950	1.674	488.23
7th Point	4,010	1.502	491.22
8th Point	4,075	1.375	492.26
9th Point	4,155	1.284	497.82

Table 3-2: Modal Parameters of the Original and the Generated FRF

	Natural Frequency [Hz]	Damping Ratio	Modal Constant
Original FRF	500	0.05	0.025
Generated FRF	520	0.1259	0.0239

There is some difference between the modal parameters of the original and the generated FRFs. However, the difference is not large enough to say that the inverse stability analysis is not applicable. Some error is expected since the stability diagram is generated from the original FRF with a software in which certain assumptions and approximations are made. Therefore, it is safe to say that inverse stability method is applicable to our problem.

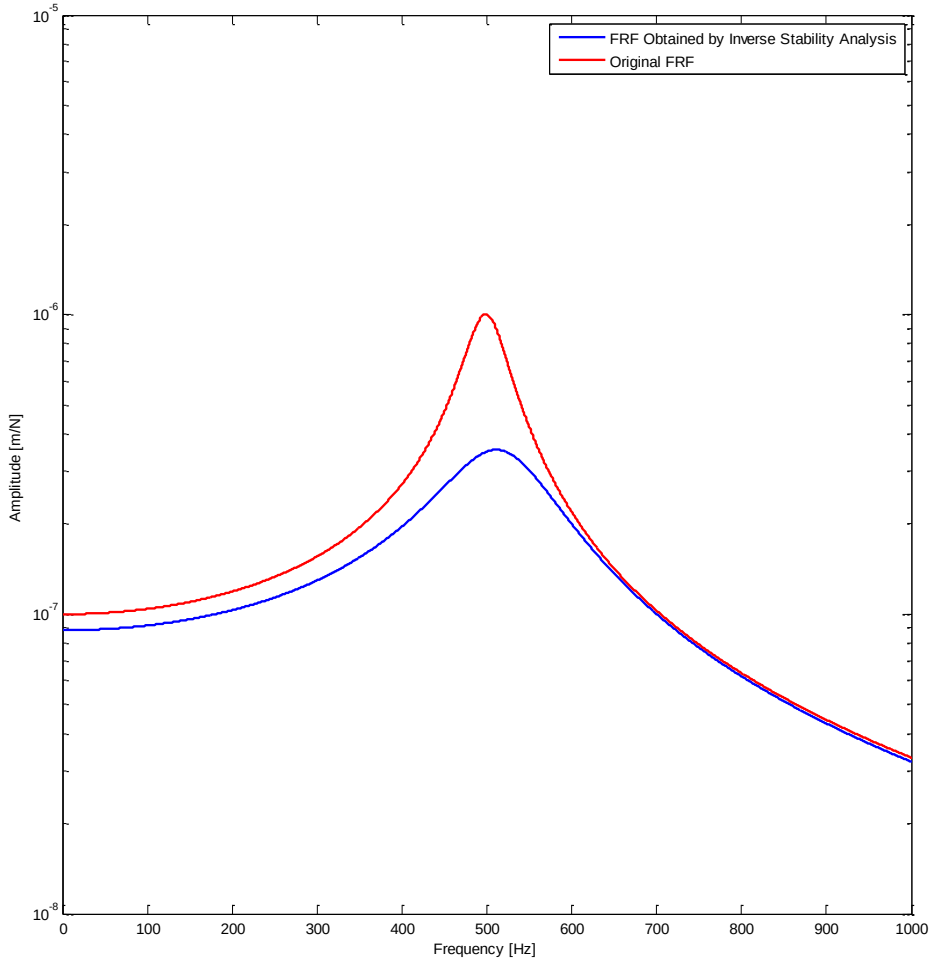

Figure 3-1: Original FRF vs. Generated FRF

CHAPTER 4

UPDATING MATHEMATICAL MODEL BY USING EXPERIMENTALLY OBTAINED TOOL POINT FRF

4.1 Chatter Detection Experiments

In conventional milling a loud noise can be heard when chatter occurs. Therefore human ear is enough to detect chatter in conventional milling. However, in micro-milling the sound generated by chatter has a very low volume, in fact the noise of the micro-machining center itself is very loud compared to chatter. Due to this fact it is usually not possible to recognize chatter with ear in micro-milling. Moreover, human ear can hear sounds from 20 Hz to 20,000 Hz. Chatter frequency in conventional milling is within this frequency range. However chatter can occur at much higher frequencies in micro-milling. Depending on the size of the micro tool and spindle speed it is possible for chatter to occur at frequencies reaching 100,000 Hz [18]. This is another reason why chatter detection cannot be performed with human ear. Several sensors are suggested for chatter detection in literature. Hendricks et al. [26] compared the performance of accelerometer, microphone and acoustic emission sensor in terms of chatter detection for high speed milling. Since the inverse stability analysis explained in Chapter 3 depends on the knowledge of chatter frequency, accurate chatter detection is an essential part of this study. In the earlier studies performed in

the Machining Research Laboratory of Sabancı University chatter detection has been proved to be problematic [22]. Measurements from acoustic emission sensor and microphone had too much noise and thus chatter could not be detected. The main cause for the inability to detect chatter was assumed to be the noise generated from the machining center itself. At the time of the previous study there was not a specialized micro-machining center in the laboratory. Therefore the experiments were performed on conventional milling machines. Since the sound measurements were inadequate for chatter detection, surface created by the micro-milling process was inspected for chatter signs. The chatter signs were present on the machined surface; however, the signs only became clear for the cases where the depths of cut were much higher than the expected stability limit. However, with this approach it is only possible to detect whether chatter occurs or not. This method gives no information about the chatter frequency which is needed to perform inverse stability analysis. Therefore, it was necessary to establish a way to detect chatter before chatter experiments could be performed. In this study a machining center which is specialized for micro-milling is utilized in the experiments. The machining center is also moderately isolated from the rest of the laboratory to reduce the environmental noise.

Figure 4-1: KERN Micro Milling Center Used in the Experiments

The performances of various sensors suggested in the literature for chatter detection were tested. In the first set of experiments a micro-mill with 1mm diameter was used. At spindle speed of 20,000 rpm slotting operation was repeated four times at different depth of cuts. The workpiece material used in the experiments was AISI 1045 steel. The feed was 2 μm per cutting tooth.

Table 4-1: Depths of Cut of the First Set of Chatter Detection Experiments

	Depth of Cut
Test 1	0.1 mm
Test 2	0.2 mm
Test 3	0.3 mm
Test 4	0.4 mm

The setup for the chatter detection test is illustrated in Figure 4-2.

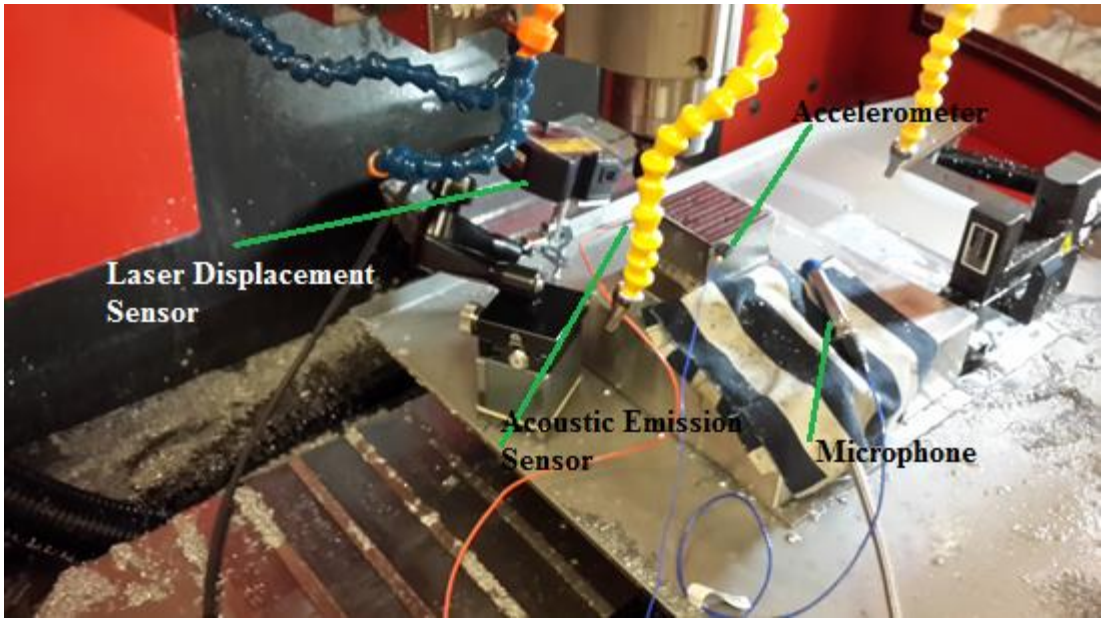

Figure 4-2: Setup for Chatter Detection Experiments

A laser displacement sensor, an accelerometer, an acoustic emission sensor and a microphone are placed as shown in Figure 4-2. Data acquisition is handled with CutPro 9.3 software. A Fourier transform is applied with the software to obtain the frequency

content of the sensory data. The frequency contents of the data acquired from acoustic emission sensor for each test are shown in Figures 4-3, 4-4, 4-5, 4-6.

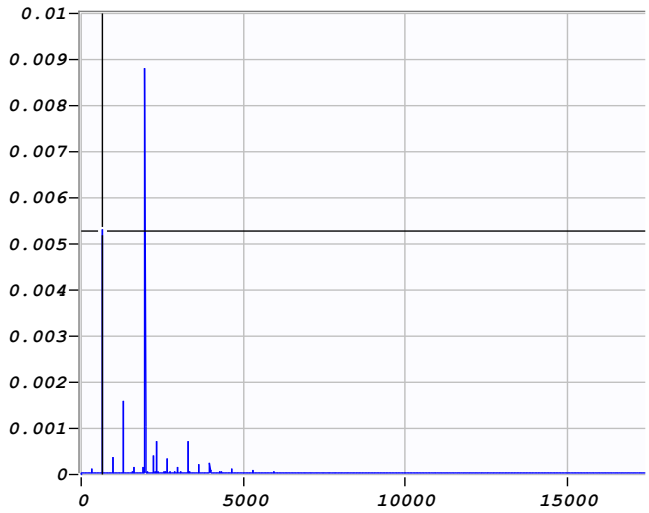

Figure 4-3: Frequency Spectrum of the Acoustic Emission Measurement of Test 1

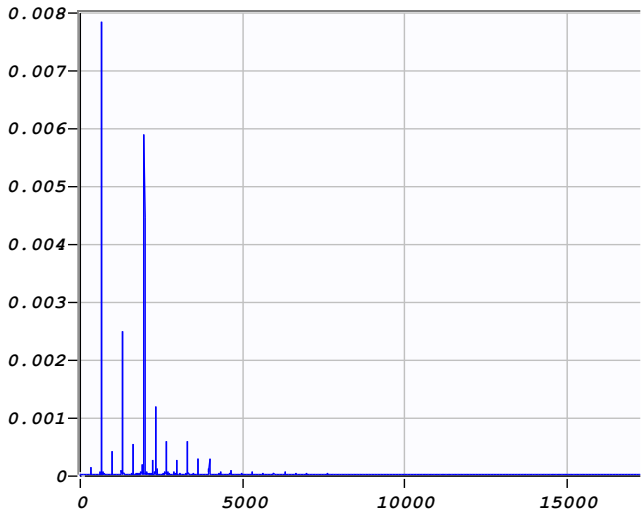

Figure 4-4: Frequency Spectrum of the Acoustic Emission Measurement of Test 2

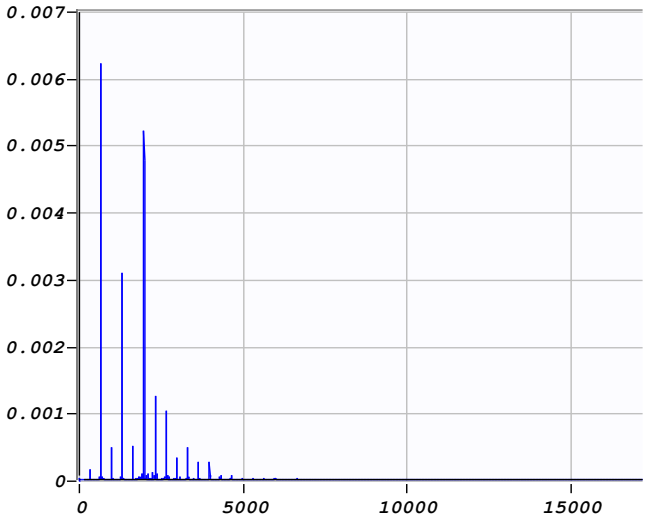

Figure 4-5: Frequency Spectrum of the Acoustic Emission Measurement of Test 3

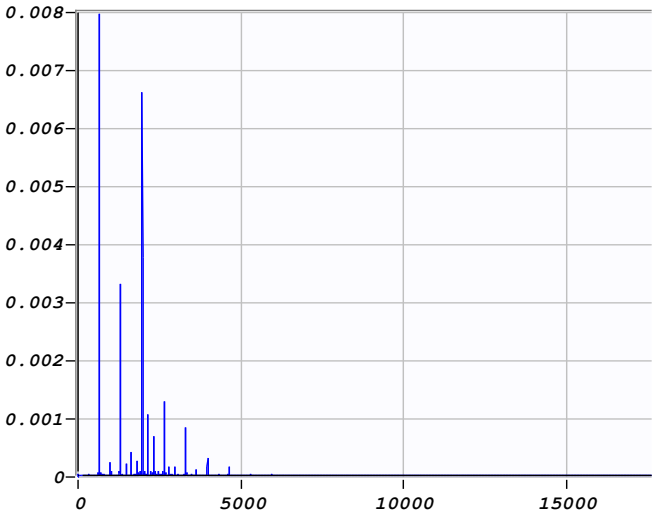

Figure 4-6: Frequency Spectrum of the Acoustic Emission Measurement of Test 4

In all 4 tests acoustic emission sensor yielded peaks at the frequency of 666 Hz and its harmonics. This frequency is the tooth passing frequency of the two fluted cutting tool rotating at 20,000 rpm. There is no indication of chatter in the frequency content of the acoustic emission signal.

The frequency contents of the microphone signals for four tests are shown in Figures 4-7, 4-8, 4-9, 4-10.

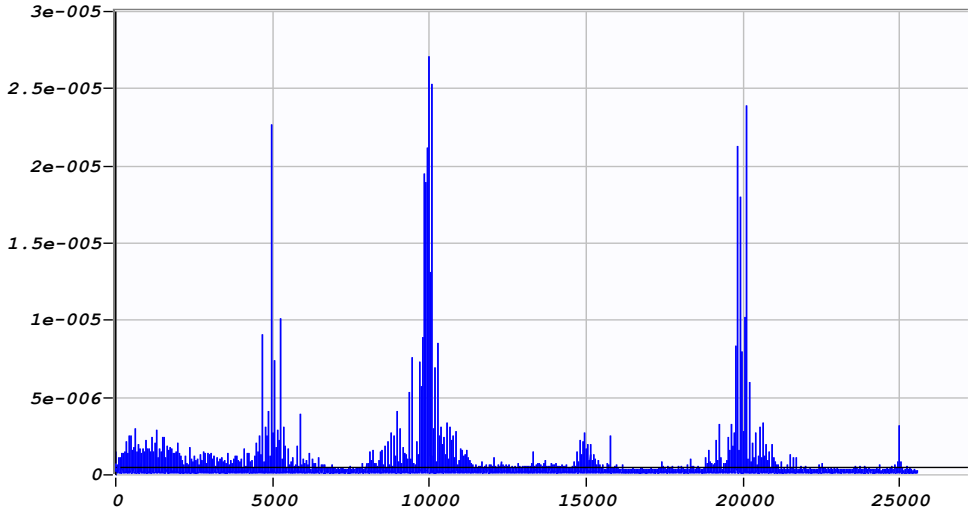

Figure 4-7: Frequency Spectrum of the Microphone Measurement of Test 1

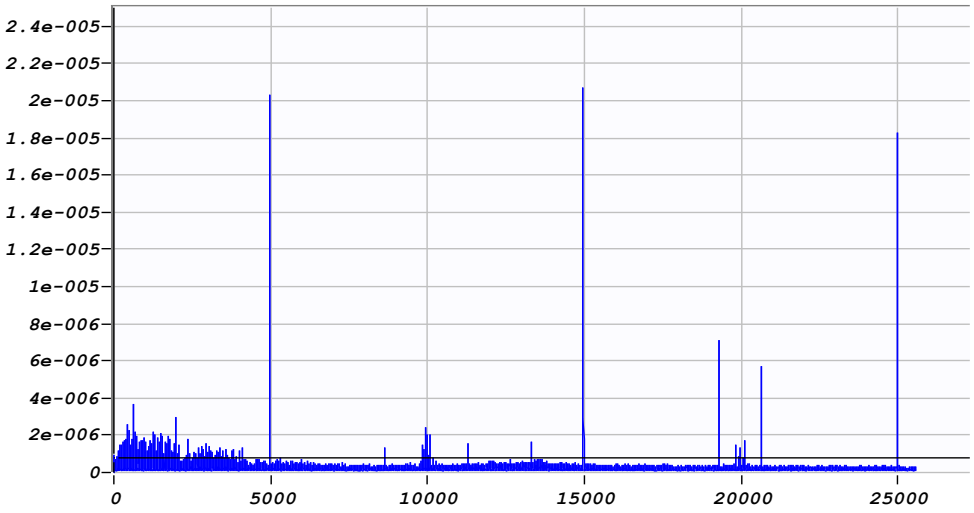

Figure 4-8: Frequency Spectrum of the Microphone Measurement of Test 2

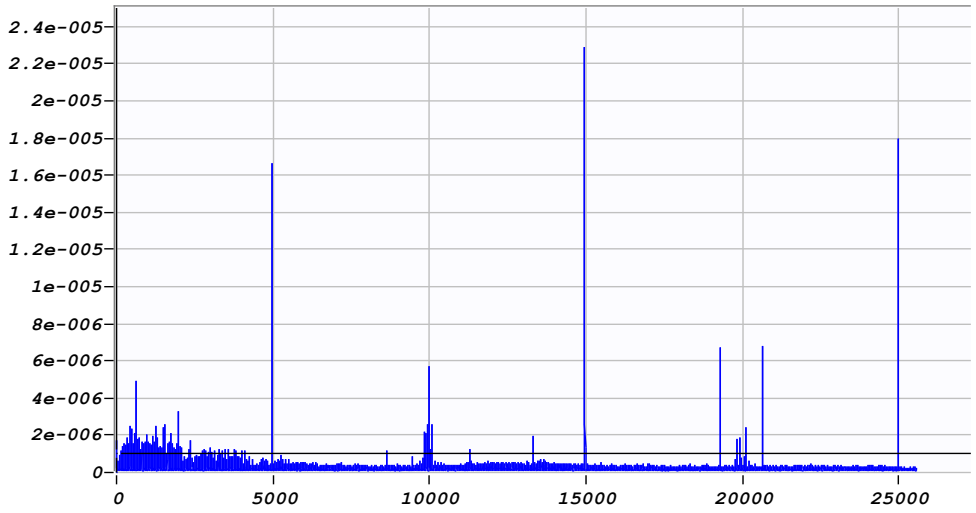

Figure 4-9: Frequency Spectrum of the Microphone Measurement of Test 3

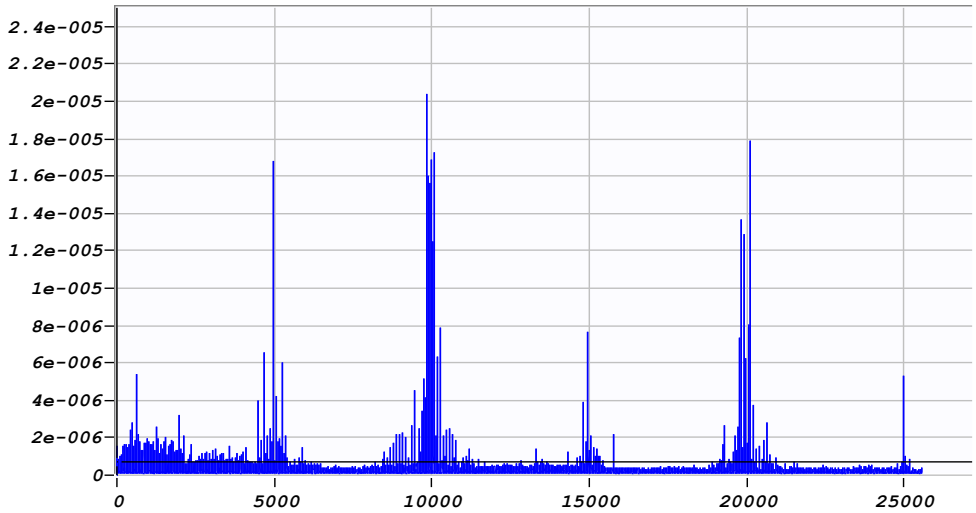

Figure 4-10: Frequency Spectrum of the Microphone Measurement of Test 4

There are peaks around 5,000 Hz and its multiples in the frequency content of microphone signal in all four tests. Although peaks at 666 Hz and its multiples also exist, their amplitude is lower compared to the peaks at multiples of 5,000 Hz. Therefore, microphone signals indicate chatter around 5,000 Hz.

The frequency content of the accelerometer signal for four tests are shown in Figures 4-11, 4-12, 4-13, 4-14.

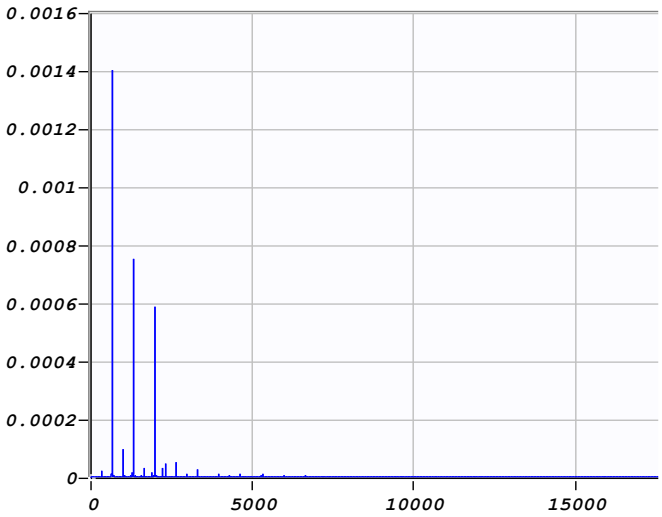

Figure 4-11: Frequency Spectrum of the Accelerometer Measurement of Test 1

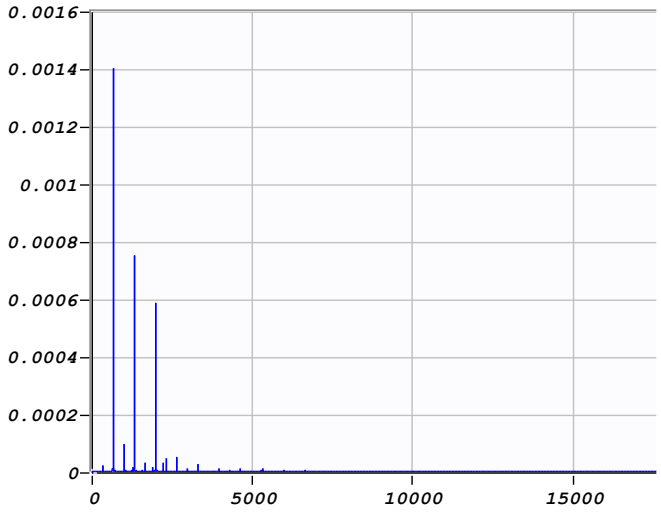

Figure 4-12: Frequency Spectrum of the Accelerometer Measurement of Test 2

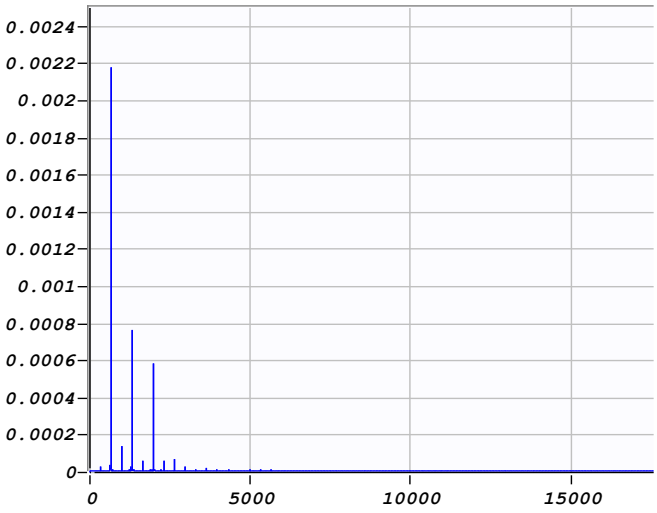

Figure 4-13: Frequency Spectrum of the Accelerometer Measurement of Test 3

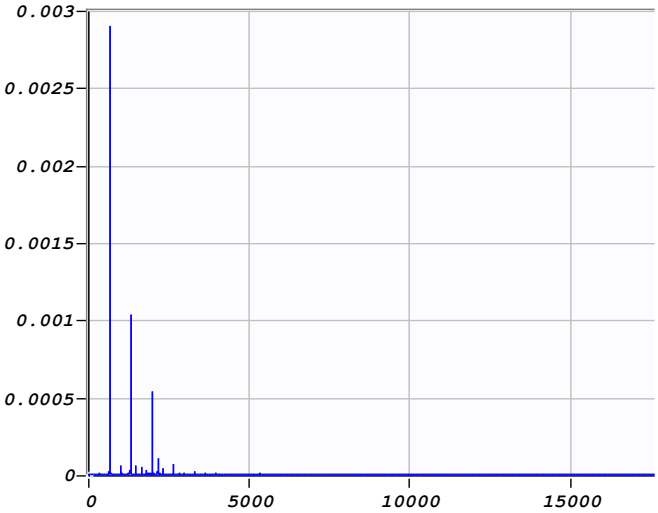

Figure 4-14: Frequency Spectrum of the Accelerometer Measurement of Test 4

Similar to acoustic emission signal, the frequency content of the accelerometer signals show peaks only at multiples of 666 Hz. Therefore there is no indication of chatter in the accelerometer data.

Unlike other three sensors, no meaningful data were obtained from laser displacement sensor.

In all four tests only the microphone signals indicated that chatter occurred, while acoustic emission sensor and accelerometer could only detect the tooth passing frequency. It should be noted that the cutting tool used in the experiments has 1 mm diameter which can be considered relatively large in micromachining. The reasoning behind choosing a cutting tool at this size is that, large tools produce louder sounds during chatter and therefore it would be easier to detect. Since the primary objective for this experiment was to detect chatter it was decided to use a large micro-mill. For a tool with 1 mm diameter microphone proved to be the ideal sensor. In order to determine whether microphone was an ideal chatter detection sensor for smaller cutting tools or not, another set of experiments were performed. An accelerometer and, an acoustic emission sensor along with a microphone were utilized again for the second set of experiments. Slotting operation was performed on AISI 1050 steel at 20,000 rpm spindle speed. The micro-mill used had a diameter of 0.6 mm. Feed rate was 2 μm per cutting tooth of the tool. Five tests at different depths of cut are performed.

Table 4-2: Depths of Cut of the Second Set of Chatter Detection Experiments

	Depth of Cut
Test 1	0.010 mm
Test 2	0.025 mm
Test 3	0.050 mm
Test 4	0.100 mm
Test 5	0.200 mm

The frequency contents of the acoustic emission signals for five tests are shown in Figures 4-15, 4-16, 4-17, 4-18, 4-19.

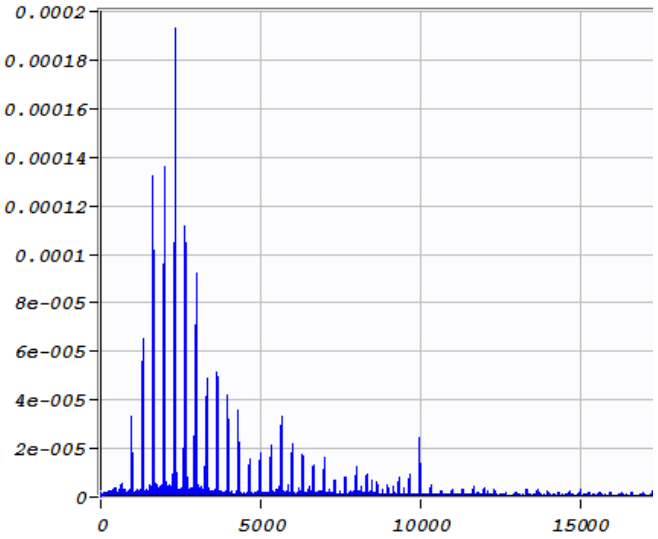

Figure 4-15: Frequency Spectrum of the Acoustic Emission Measurement of Test 1

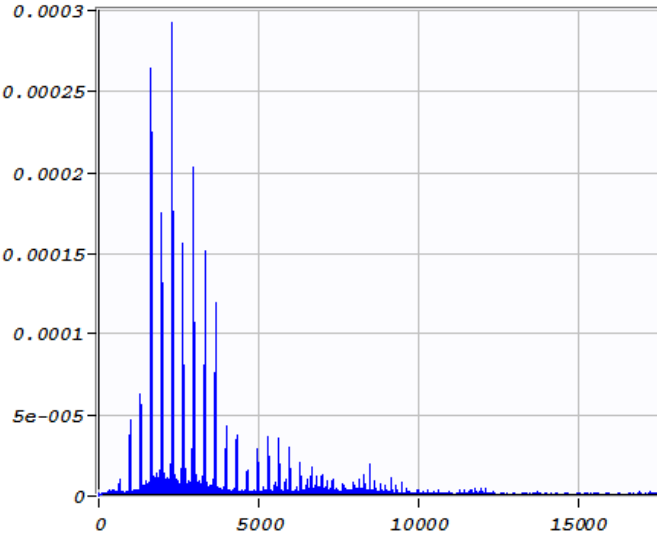

Figure 4-16: Frequency Spectrum of the Acoustic Emission Measurement of Test 2

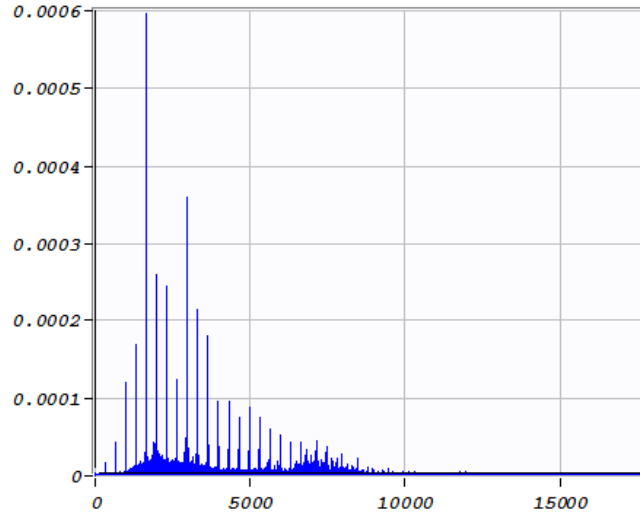

Figure 4-17: Frequency Spectrum of the Acoustic Emission Measurement of Test 3

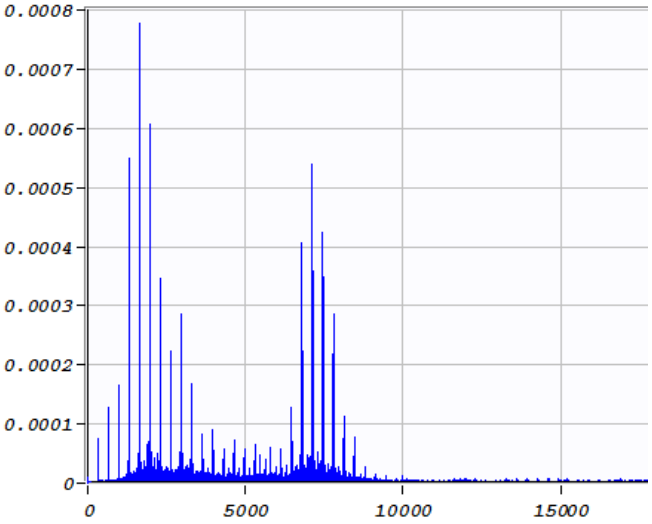

Figure 4-18: Frequency Spectrum of the Acoustic Emission Measurement of Test 4

In the frequency content of the acoustic emission signals, peaks can be observed in 333Hz and its harmonics. These are the spindle rotation and tooth passing frequencies. Beside these frequencies, however, frequency content of the signal from test 4 and test 5 show peaks at different frequencies. In test 4 and test 5 peaks at 7,080 Hz are detected. This frequency is not a multiple of the tooth passing frequency. Therefore, it can be concluded that chatter has occurred at this frequency. In the frequency content

of the signals for tests 1 to 3 no peaks are observed at 7,080 Hz. This means that the cutting operations in those cases were stable and no chatter occurred. By increasing the depth of cut from 0.050 mm to 0.100 mm, the limiting depth of cut was exceeded. Finally, it can be concluded that the acoustic emission sensor was capable of detecting chatter for this case.

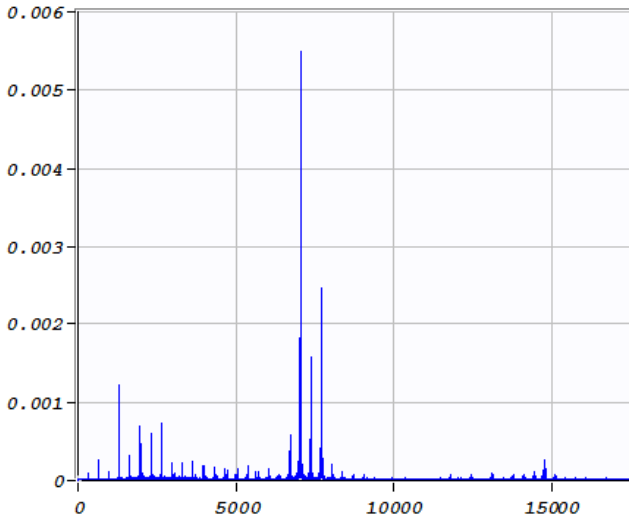

Figure 4-19: Frequency Spectrum of the Acoustic Emission Measurement of Test 5

The frequency content of the microphone signals for the five tests are shown in Figures 4-20, 4-21, 4-22, 4-23, 4-24.

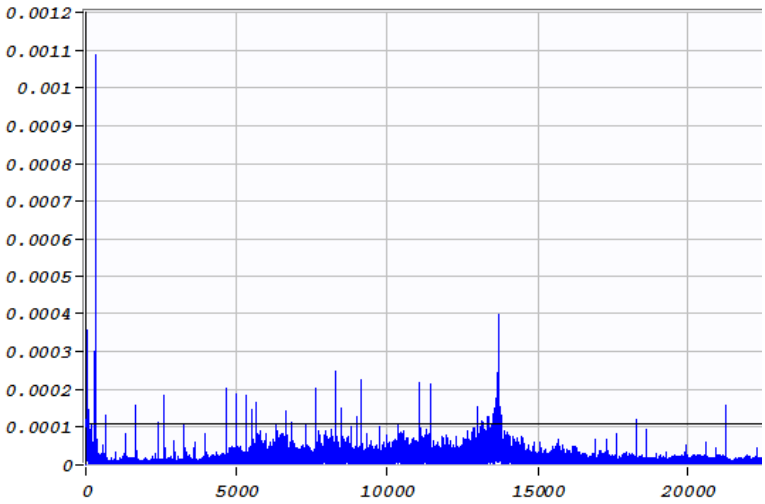

Figure 4-20: Frequency Spectrum of the Microphone Measurement of Test 1

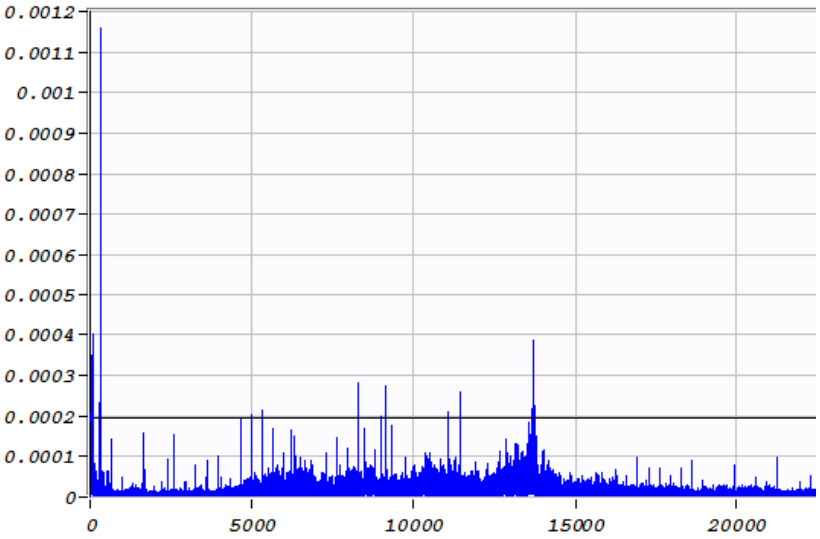

Figure 4-21: Frequency Spectrum of the Microphone Measurement of Test 2

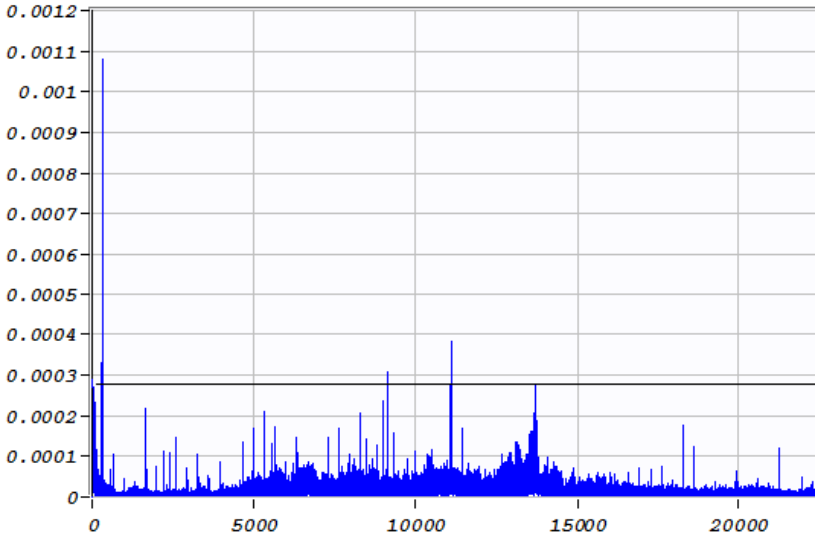

Figure 4-22: Frequency Spectrum of the Microphone Measurement of Test 3

As was seen in the acoustic emission signals, in test 4 and test 5 chatter frequency is detected at 7,080Hz and only tooth passing frequency is observed in the signals from tests 1 to 3. However, only in test 5 chatter is clearly visible in microphone signal. In the frequency content of signal 4 there are several peaks, in other words the signal is very noisy. It can be concluded that, microphone is less sensitive to chatter sound than

acoustic emission sensor, since microphone signal showed chatter clearly only at a larger depth of cut.

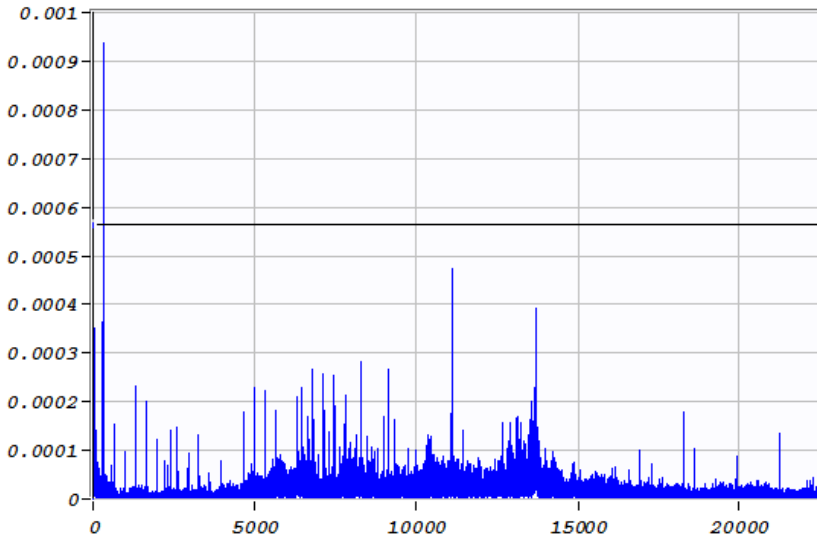

Figure 4-23: Frequency Spectrum of the Microphone Measurement of Test 4

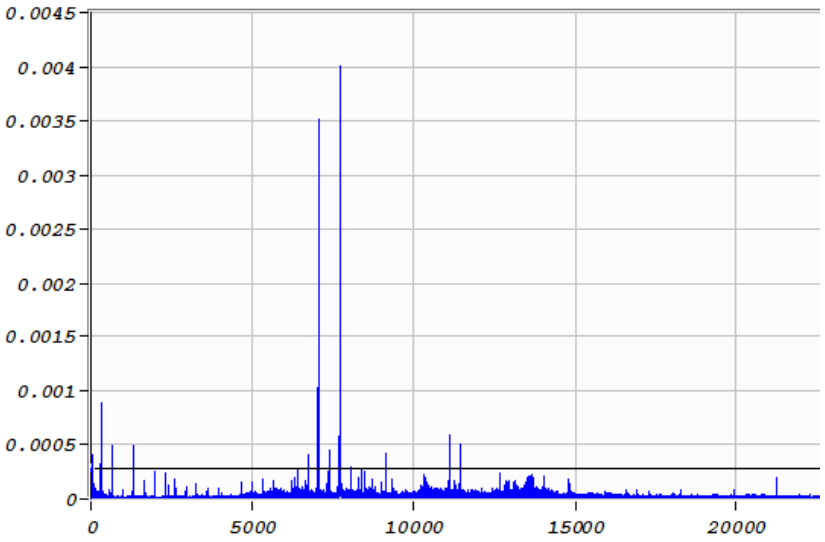

Figure 4-24: Frequency Spectrum of the Microphone Measurement of Test 5

The frequency content of the accelerometer signals for the five tests are shown in Figures 4-25, 4-26, 4-27, 4-28, 4-29.

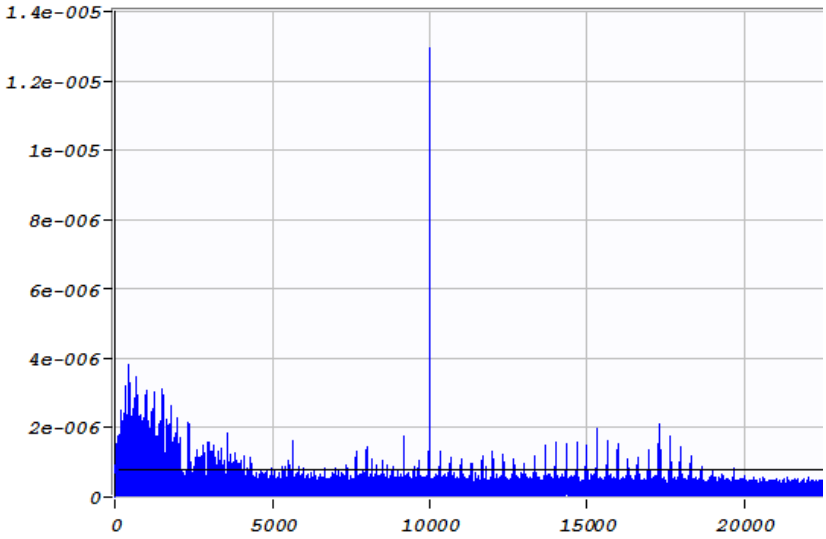

Figure 4-25: Frequency Spectrum of the Accelerometer Measurement of Test 1

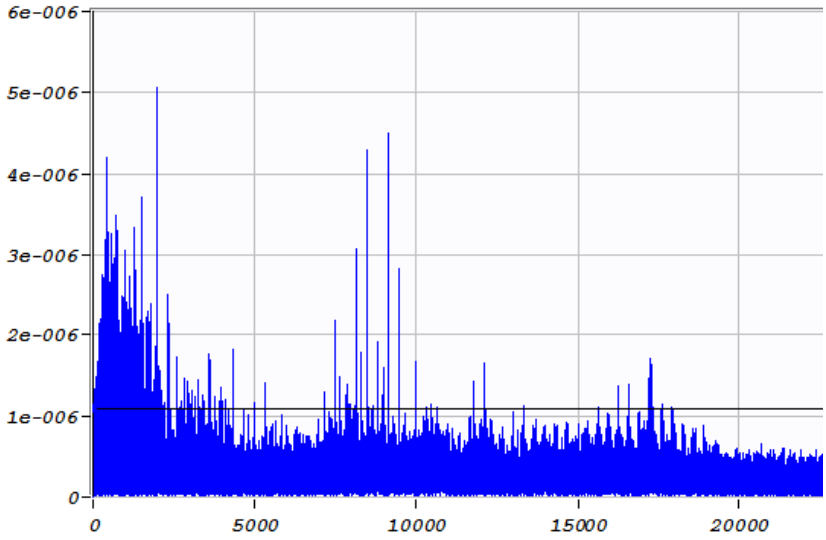

Figure 4-26: Frequency Spectrum of the Accelerometer Measurement of Test 2

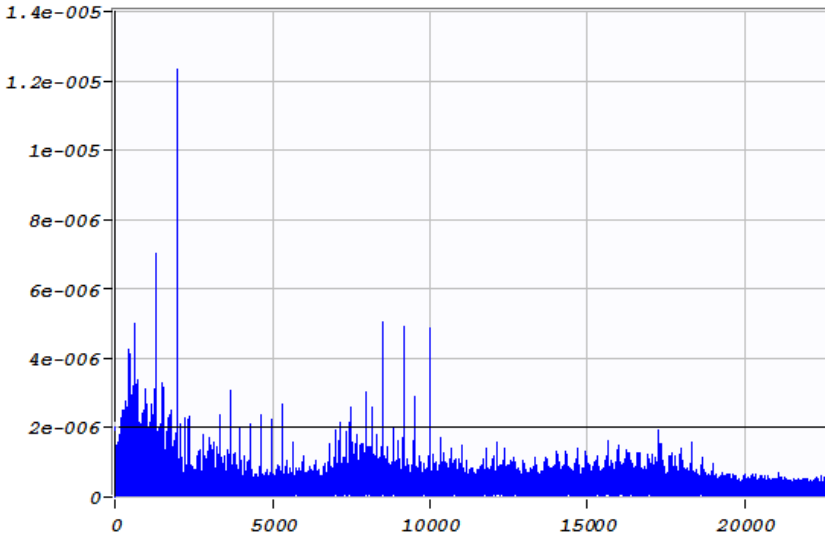

Figure 4-27: Frequency Spectrum of the Accelerometer Measurement of Test 3

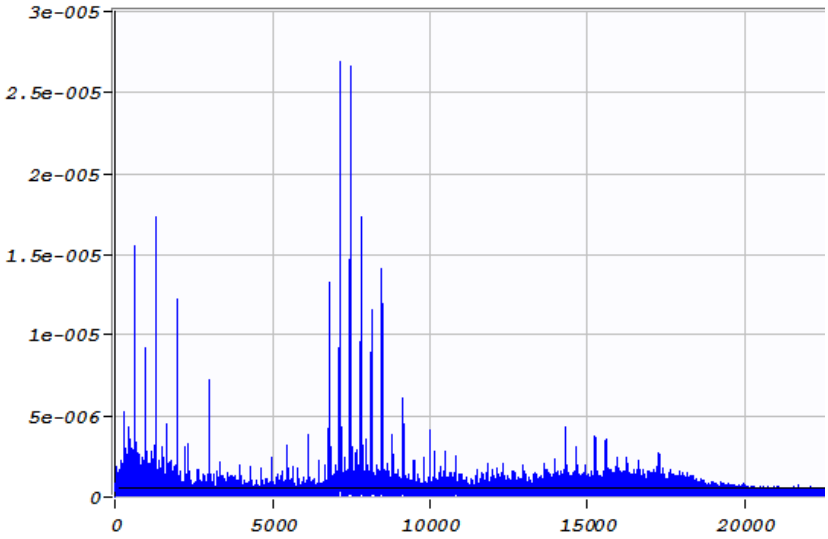

Figure 4-28: Frequency Spectrum of the Accelerometer Measurement of Test 4

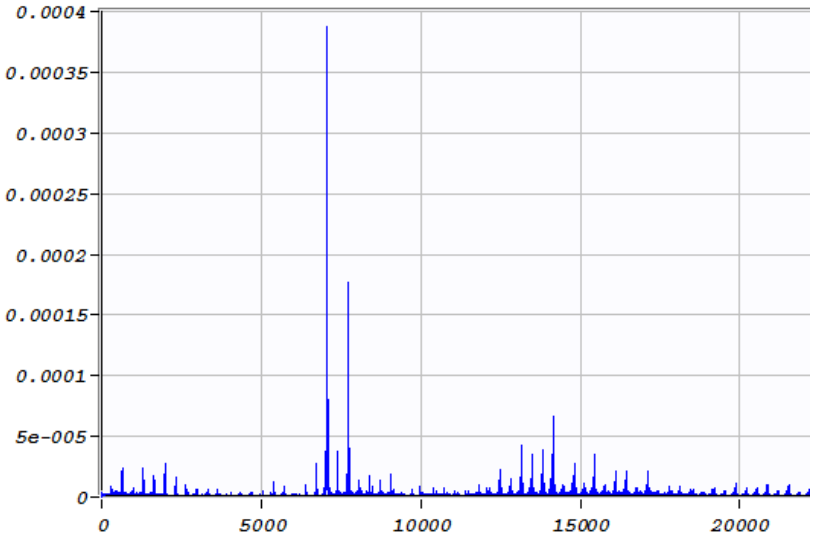

Figure 4-29: Frequency Spectrum of the Accelerometer Measurement of Test 5

The frequency contents of accelerometer signals are very similar to frequency contents of the acoustic emission signals. The chatter occurring at 7,080 Hz can be clearly observed in the signals of test 4 and test 5.

In the first set of experiments where 1mm diameter tool was used, chatter could only be detected by the microphone. However, in the second set of experiments conducted with a 0.6mm diameter tool a different conclusion was arrived at. When a smaller tool was used acoustic emission sensor and accelerometer signals showed clear signs of chatter. While the microphone signal still showed signs of chatter for the smaller tool, the frequency content of microphone signal was noisier. The experiments show that microphone is better at detecting chatter when the tool is larger and it becomes less capable of detecting chatter as the tool gets smaller. On the other hand, acoustic emission sensor and accelerometer is better at detecting chatter for smaller tools. Therefore, it is concluded that using a combination of sensors is the best approach to secure chatter detection in future experiments.

4.2 Chatter Experiments

In order to update the theoretical model several chatter tests were performed on a micro milling center. The parameters of the performed tests are given in Table 4-3.

Table 4-3: Parameters of the Chatter Experiment

	Spindle Speed	Depths of Cuts
Test 1	19,000 rpm	50 µm, 100 µm
Test 2	20,000 rpm	5 µm, 25 µm, 50 µm, 100 µm, 200 µm
Test 3	21,000 rpm	50 µm, 100 µm,
Test 4	25,000 rpm	5 µm, 50 µm, 100 µm, 200 µm
Test 5	30,000 rpm	5 µm, 50 µm, 100 µm
Test 6	35,000 rpm	50 µm, 100 µm
Test 7	40,000 rpm	50 µm, 100 µm

The experimental setup is shown in Figure 4-30.

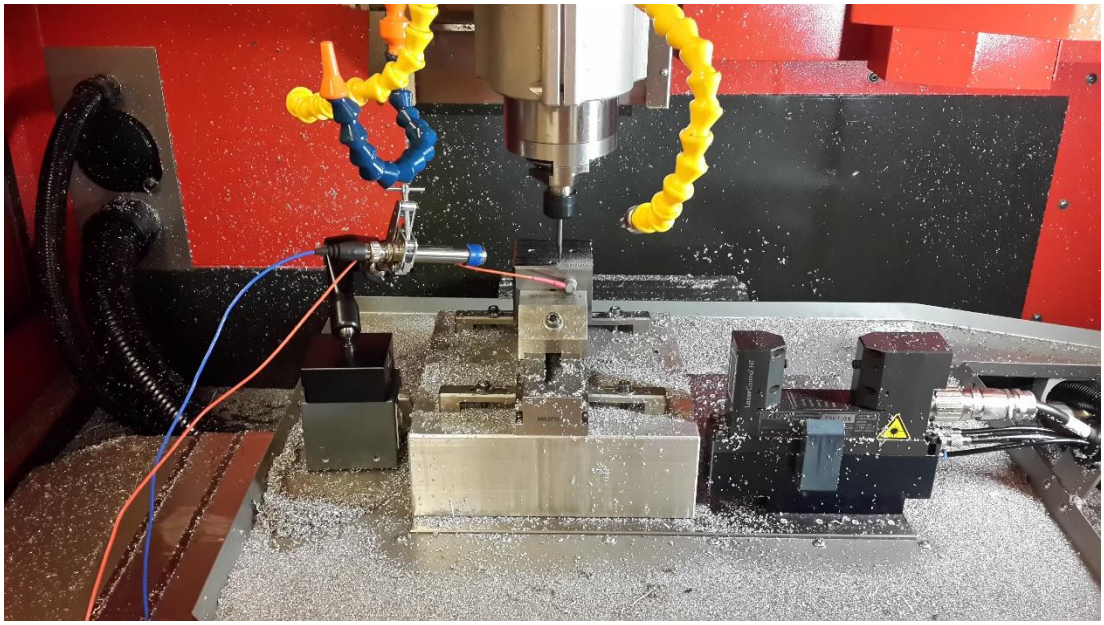

Figure 4-30: Experimental Setup for the Chatter Tests

The tool used in the experiment had 0.6mm diameter. The workpiece material was AISI1050 steel. An acoustic emission sensor and a microphone were used as sensors to record the sound throughout the cutting process. A Fourier transform was performed on the sound data using CutPro 9.3 software. Frequency content of the recorded sounds were inspected to determine whether chatter occurred or not. Frequency of the spindle rotation and its multiples always exist within the frequency content of the sound data. In some tests however, there exist large peaks in the frequencies not located at multiples of the spindle rotation frequency. When such peaks are observed in the frequency content of the sound data, chatter is confirmed and the frequency where the peak is located is declared as the chatter frequency. The result of the chatter tests are given in Table 4-4.

Table 4-4: Chatter Frequencies Obtained From the Tests

	5 μm	25 μm	50 μm	100 μm	200 μm
19,000 rpm	-	-	3,480 Hz	3,613 Hz	-
20,000 rpm	No chatter	No chatter	3,559 Hz	3,603 Hz	3,755 Hz
21,000 rpm	-	-	3,613 Hz	3,652 Hz	-
25,000 rpm	No chatter	-	3,614 Hz	3,649 Hz	3,780 Hz
30,000 rpm	No chatter	-	3,785 Hz	3,777 Hz	-
35,000 rpm	-	-	No chatter	3,873 Hz	-
40,000 rpm	-	-	3,846 Hz	3,910 Hz	-

By applying the inverse stability method to data obtained from chatter tests, it is possible to obtain the model parameters for the dominant mode. It should be noted that the solution method can be unstable and heavily depends on the initial conditions.

In order to perform inverse stability analysis three data points are selected. From the 3 data points 6 nonlinear equations are obtained. These 6 nonlinear equations are solved using the least squares method for the 3 unknown modal parameters. The data used in the analysis are shown in Table 4-5. The modal parameters are found as shown in Table 4-6.

Table 4-5: Test Points Used in Inverse Stability Analysis

	1st Point	2nd Point	3rd Point
Spindle Speed [rpm]	19,000	20,000	21,000
Depth of Cut [μm]	100	200	100
Chatter Frequency [Hz]	3,613	3,755	3,652

Table 4-6: Modal Parameters Obtained with Inverse Stability Analysis

Natural Frequency [Hz]	3,511
Damping Ratio	0.1121
Modal Constant	39.74

The modal parameters presented in Table 4-6 are then used to generate the stability diagram given in Figure 4-31.

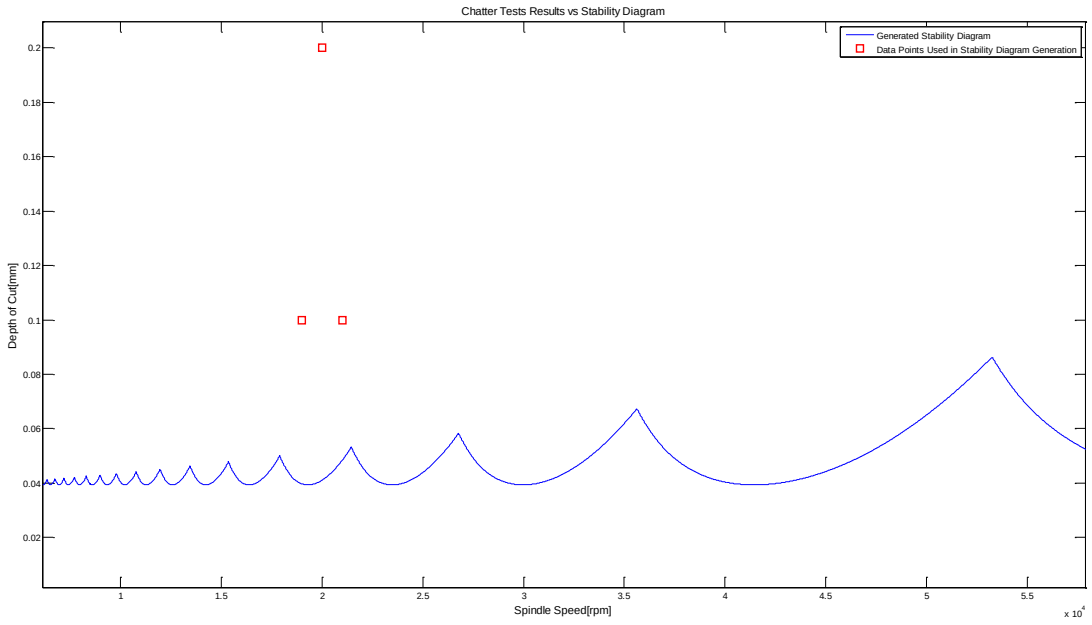

Figure 4-31: Stability Diagram Generated After Inverse Stability Analysis

In Figure 4-31, red squares represent the data points used in the inverse stability analysis to obtain the modal parameters. Stability diagrams predict that chatter occurs above the curve and stable operation only happens below the curve. The selected points remain above the generated stability curve as expected. Therefore the method remains valid.

The generated stability curve is then compared with the remaining chatter tests data given in Table 4-4. The Figure 4-32 shows all the chatter test data and the generated stability diagram.

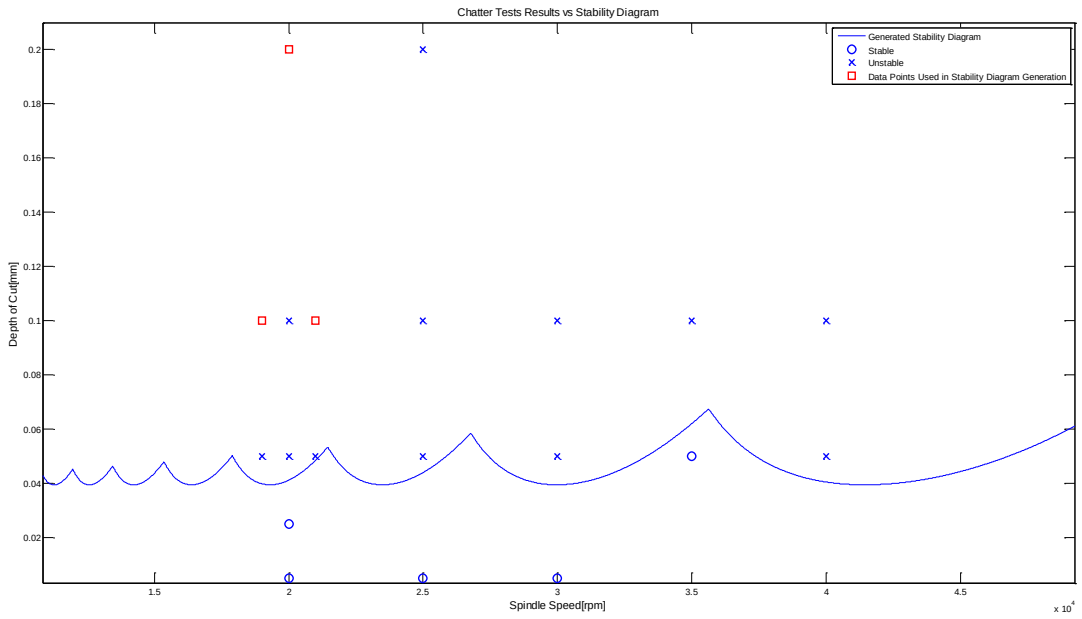

Figure 4-32: Chatter Tests vs. Stability Diagram

The red squares are the data points used in the inverse stability analysis as before. The stars indicate the cases where chatter was detected. The circles indicate that no chatter was detected at that point and that the operation was stable. Since all the cases where chatter occurred remains above the predicted stability curve whereas all the cases where no chatter occurred remain below the stability curve, there is no conflict between experiments and the stability diagram. Thus, using 3 data points from the chatter experiments, stability diagram was accurately generated.

4.3 Comparison of Analytical FRF and Experimentally Obtained FRF

The mathematical model requires the geometric information of the cutting tool as well as its material properties. The cutting tool is connected to the tool holder as shown in Figure 4-33.

Figure 4-33: Cutting Tool and Tool Holder Assembly

The tool material is carbide. Material properties of the tool are taken as follows; mass density ρ=14300 kg/m^3, Young's modulus E=580 GPa, Poisson's ratio ν=0.28 and structural damping ratio γ=0.01. The geometrical properties of the holder and tool are given in Table 4-7 and Table 4-8, respectively.

Table 4-7: Holder Dimensions

Segment Number	1	2	3	4	5	6	7
Length (mm)	18.5	3.65	5.8	2.8	3.2	1.9	3.2

Outer Diameter (mm)	25	18.63	26.05	26.05	32.96	27.08	32.96
Inner Diameter (mm)	4	4	4	4	4	0	13.93

Table 4-8: Tool Dimensions

Segment Number	1	2	3	4	5	6	7	8	9
Length (mm)	1.6	0.6	1.6	1.6	1.6	1.6	1.6	1.7	27.1
Outer Diameter (mm)	0.402	0.6	0.8	1.2	1.8	2.2	2.8	3.2	4

The theoretical FRF and the FRF obtained from the inverse stability analysis are shown in the Figure 4-34.

As seen in the Figure 4-34, there is considerable difference between two FRFs. Biggest difference is the nonexistence of the other modes in the experimental FRF. The reason why there is only one mode in the experimentally identified FRF is that, inverse stability analysis only yields the modal parameters of the most dominant mode responsible for chatter. This is an expected outcome since the higher modes which are lower in amplitude are not important for stability. Therefore, the difference between two FRFs, other than the first and the most significant mode for this case is not important from chatter stability prediction stand point. However, the error in the first mode of the FRFs is also considerably large. The error, in this case is caused by several factors. First of all, the theoretical model used in the FRF determination was not developed for the micro cutting tools. The assumptions in the model were made

considering larger machining tools. Moreover, possible measurement errors in the experiments are another source for the difference between the two FRFs. Errors arising from the numerical solution are also another cause for the difference between FRFs. While there are many possible sources for errors, the focus at this point is to improve the theoretical model so that a better fit between two FRFs can be obtained. To this end, the parameters in the mathematical model are updated and compared with the experimental FRF. The damping ratio of 0.05 is used for cutting tool material in the theoretical model. Since the first mode of experimental FRF is more damped than that of the theoretical FRF, the damping ratio is increased and a new FRF is generated. The updated theoretical FRF and the experimental FRF are shown in Figure 4-35.

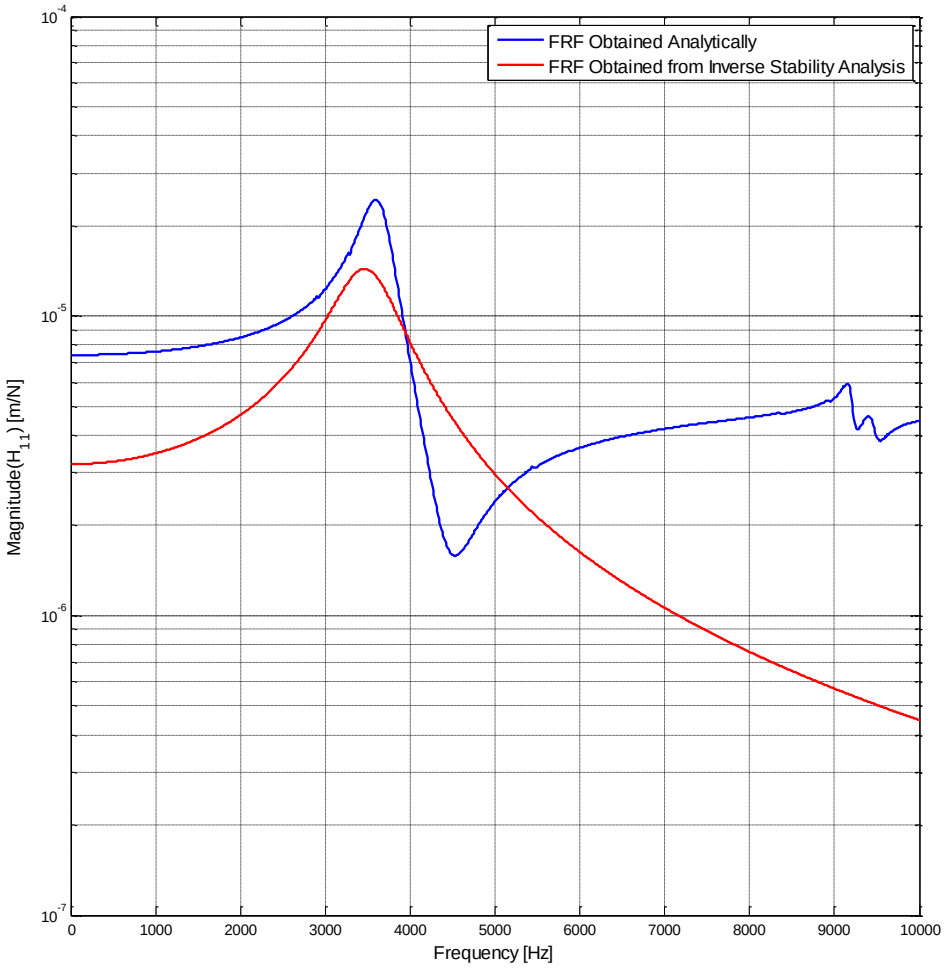

Figure 4-34: Analytical vs. Experimental FRF

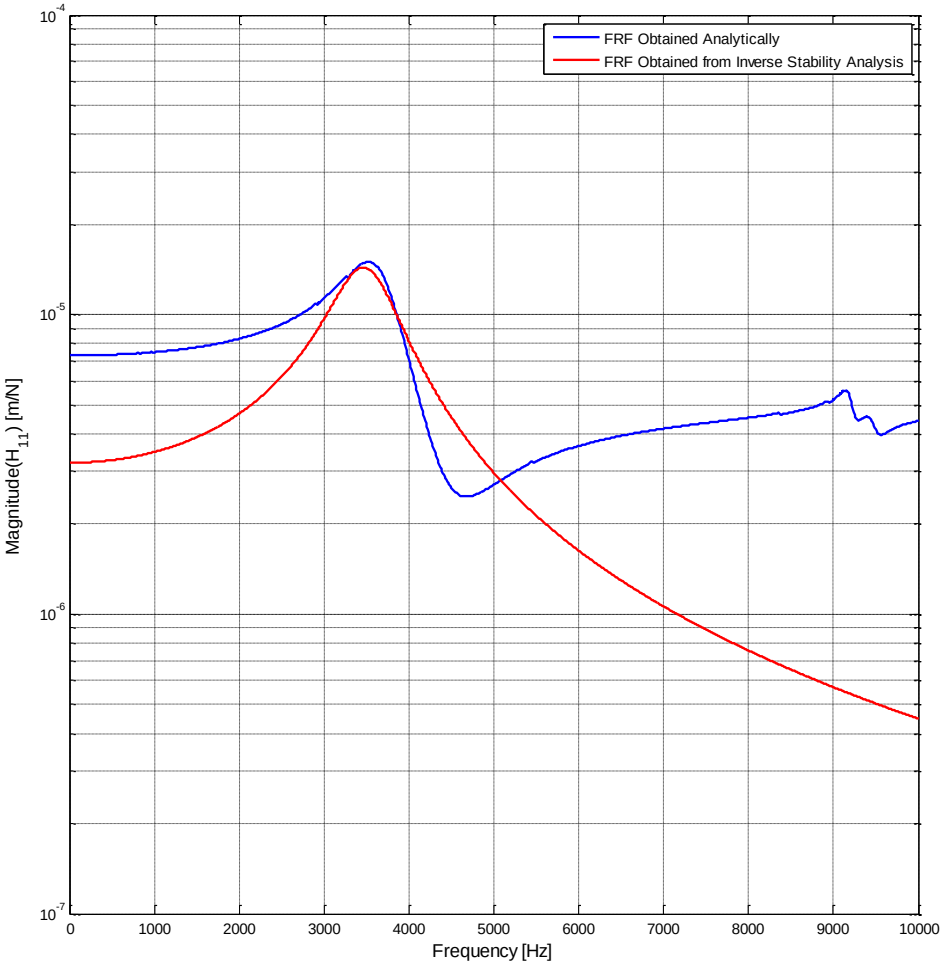

Figure 4-35: Updated Analytical FRF vs. Experimental FRF

In Figure 4-35 the error in the first mode is lower compared to Figure 4-34. The other material property that can be updated is the elastic modulus of the cutting tool. However, increasing or decreasing the elastic modulus of the cutting tool shifts the first mode either left or right. Although changing elastic modulus also affects the amplitude, the change it causes in natural frequency is higher in comparison. Comparing Figure 4-35 with Figure 4-36, it can be seen that modifying the damping ratio yielded better results. Therefore, it was concluded that the damping ratio of the tool should be increased in the theoretical model.

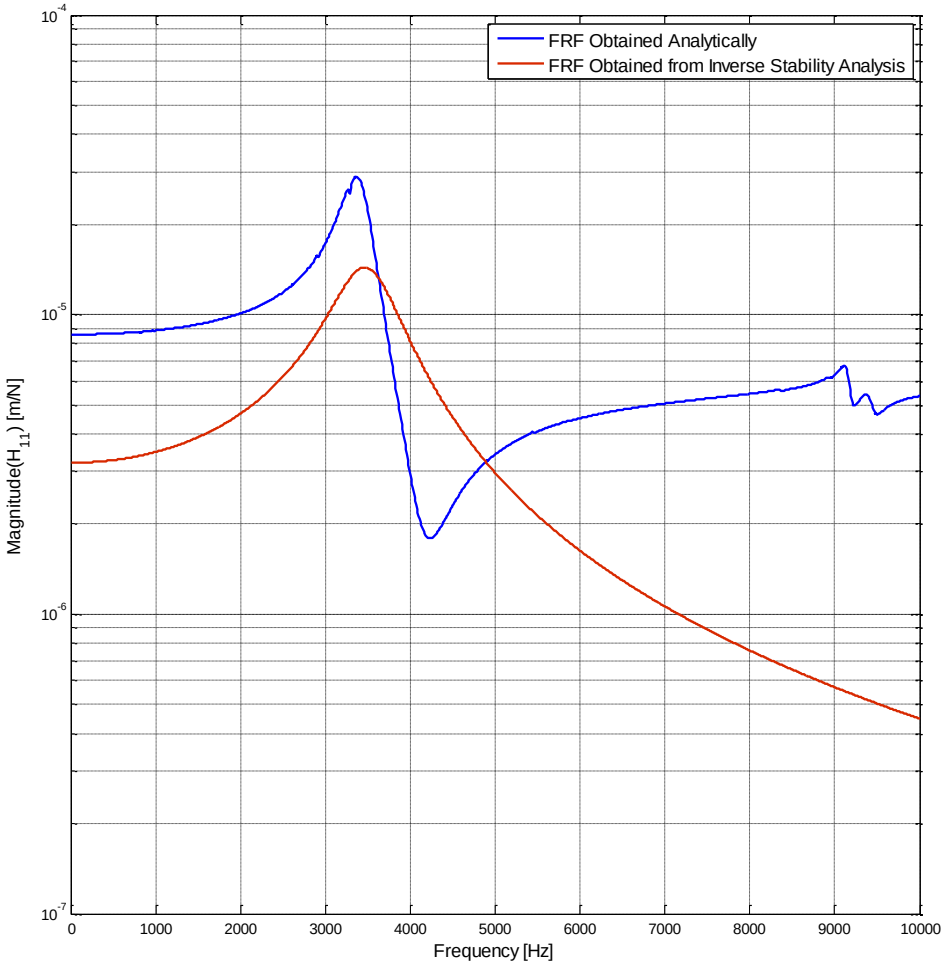

Figure 4-36: Updated Analytical FRF vs. Experimental FRF

CHAPTER 5

CONCLUSIONS

Micro milled products have very high precision requirements. In order to meet these requirements, a cutting operation without chatter must be performed. As commonly known, chatter vibrations result in poor surface finish and reduced tool life. In order to have a stable milling operation without chatter, an accurate stability diagram must be generated, which requires an accurate tool point FRF. In this thesis, a theoretical model for determining the tool point FRF of a micro machining center is presented. Theoretical model for obtaining the tool point FRF developed by Ertürk et al. [9], was extended to include gyroscopic effects by Özşahin et al. [23]. The inverse stability analysis presented and proven by Özşahin et al. [23] as well as all the formulations are modified for the micro milling in this study. Thus, a modified version of the method for micro milling to obtain modal parameters from chatter tests was introduced. Inverse stability analysis is applied for the first time to micro machining in this study. Moreover, for the first time, inverse stability method is used for tool dynamics identification. After performing numerous chatter tests, it was shown that it is possible to obtain the modal parameters using the proposed modified inverse stability analysis for micro milling operations. Next, the theoretical and experimental FRFs were compared. Finally, the theoretical model is updated by changing the properties of the cutting tool material which resulted in a better agreement with the experimental FRF.

In order to obtain the tool point FRF of a micro milling tool, an inverse stability analysis has been presented. Firstly, several experiments were performed to determine which sensor was more effective for chatter detection in micro machining. It was observed that microphone was a better sensor when the cutting tool was as large as 1mm in diameter. However, acoustic emission sensor and accelerometer gave better results when the tool was smaller. After chatter detection in micro machining was investigated and the sensors to be used in experiments were selected, chatter experiments were performed. Using the data obtained from the chatter experiments; performed with the same tool, the stability analysis was performed backwards to identify the modal parameters. The main assumption in this method is that, the tool point FRFs in x and y directions are the same. This would only hold true when the cutting tool is very small in size compared to machining center, and thus is dynamically the most flexible component in the machining system. Machining center used in this study satisfies this condition as it is significantly larger than the tool used in experiments. Another assumption made in this method is that there is only one effective mode in the tool point FRF which determines the stability diagram. This condition requires that one mode of the tool point FRF is considerably larger than the other modes. Therefore, the method would not work when there are multiple modes effecting the stability diagram. However, by appropriately choosing the overhang length of the cutting tool, it is possible to change the tool point FRF so that one mode becomes considerably larger than the rest of the modes. If these two conditions are met, then it is possible to obtain the modal parameters from the chatter test results using the inverse stability method. The method is used to determine 3 modal parameters, which are natural frequency, damping ratio and modal constant. For each chatter test two equations are obtained, and it is possible to obtain as many equations as required by simply making more experiments. Therefore, by making more experiments and spending more computational time, it is possible to obtain more accurate results by utilizing the least squares error method. Since the number of equations are not limited, it is also possible to include more modes in the calculations. For instance, one can consider different FRFs in x and y directions doubling the number of unknowns. However, increasing the number of unknowns may cause some

difficulty in calculations. Further studies in this direction is recommended as future work.

The modal parameters obtained with the inverse stability analysis are used to generate the tool point FRF. This FRF, obtained from the experimental data is then compared with the theoretically obtained FRF. Although a considerable difference is observed between the two FRFs, it was possible to obtain a better fit by updating the mathematical model which is the objective of this research. Modifying the elastic modules of the cutting tool did not yield a better fit. However, it was shown that by increasing the damping ratio of the tool from 0.05 to 0.1 a better fit could be obtained. Some part of the increase of the damping ratio can perhaps be attributed to the process damping phenomenon. Process damping is especially significant in the lower cutting speeds, which was not considered in this study in order to simplify the procedure. Therefore, it is possible that some of the increase in the damping ratio coefficient is due to the neglected process damping. This is another point that should be investigated further.

REFERENCES

[1] Y. Altintas, Manufacturing Automation, Cambridge University Press, 2000.

[2] T. Schmitz, S. Smith. Machining Dynamics: Frequency Response to Improved Productivity. s.l.: Springer, 2009.

[3] Analytical modeling of spindle-tool dynamics on machine tools using Timoshenko beam model and receptance coupling for the prediction of tool point FRF. A. Ertürk, H.N. Özgüven, Budak E. 15, s.l.: International Journal of Machine Tools and Manufacture, 2006, Vol. 46.

[4] A spectral-Tchebychev technique for solving linear and nonlinear beam equations. S. Filiz, O.B. Ozdoganlar and L.A. Romero. 8, s.l.: Journal of Vibration and Controls, 2008, Vol. 14

[5] Tool Point Frequency Response Prediction for High-Speed Machining by RCSA. Tony L. Schmitz, Matthew A. Davies, Michael D. Kennedy. s.l.: Transactions of the ASME, 2001, Vol. 123.

[6] Predicting High-Speed Machining Dynamics by Substructure Analysis. Schmitz, T. and Donaldson, R. 1, s.l.: Annals of the CIRP, 2000, Vol. 49.

[7] The Analysis of Vibrating Systems which Embody Beams. Bishop, R. E. D. s.l.: Proceedings of the Institution of Mechanical Engineers 1847-1996, 1955, Vol. 169.

[8] Receptance coupling for end mills. Simon S. Park, Yusuf Altintas and Mohammad Movahhedy. 9, s.l. : International Journal of Machine Tools and Manufacture, 2003, Vol. 43.

[9] Analytical modeling of spindle–tool dynamics on machine tools using Timoshenko beam model and receptance coupling for the prediction of tool point FRF. Budak, A. Ertürk ?. Özgüven E. s.l. : International Journal of Machine Tools & Manufacture, 2006, Vol. 46.

[10] A three-dimensional model for the dynamics of micro-endmills including bending, torsional and axial vibrations. Sinan Filiz, O. Burak Ozdoganlar. 1, s.l. : Precision Engineering, 2011, Vol. 35.,

[11] Structural modeling of end mills for form error and stability analysis. E.B. Kivanc, E. Budak. s.l. : International Journal of Machine Tools and Manufacture, 2004, Vol. 44

[12] Chae, J., Park, S. S., & Freiheit, T. (2006). Investigation of micro-cutting operations. International Journal of Machine Tools and Manufacture, 46(3-4), 313–332. doi:10.1016/j.ijmachtools.2005.05.015

[13] Effects of the Cutting Tool Edge Radius on the Stability Lobes in Micro-milling. AFAZOV, S., RATCHEV, S. and SEGAL, J.,. s.l. : Advanced Materials Research, 2011, Vol. 223.

[14] Mascardelli, B. a., Park, S. S., & Freiheit, T. (2008). Substructure Coupling of Microend Mills to Aid in the Suppression of Chatter. Journal of Manufacturing Science and Engineering, 130(1), 011010. doi:10.1115/1.2816104

[15] Chatter suppression in micro end milling with process damping. Ramin Rahnama, Mozhdeh Sajjadi, Simon S. Park. s.l. : Journal of Materials Processing Technology, 2009, Vol. 209

[16] Robust chatter stability in micro-milling operations. S.S. Park, R. Rahnama. s.l. : CIRP Annals - Manufacturing Technology, 2010, Vol. 59

[17] Tajalli, S. A., Movahhedy, M. R., & Akbari, J. (2012). Investigation of the Effects of Process Damping on Chatter Instability in Micro End Milling. Procedia CIRP, 1, 156–161. doi:10.1016/j.procir.2012.04.027

[18] Jin, X., & Altintas, Y. (2013). Chatter Stability Model of Micro-Milling With Process Damping. Journal of Manufacturing Science and Engineering, 135(3), 031011. doi:10.1115/1.4024038

[19] Afazov, S. M., Ratchev, S. M., Segal, J., & Popov, a. a. (2012). Chatter modelling in micro-milling by considering process nonlinearities. International Journal of Machine Tools and Manufacture, 56, 28–38. doi:10.1016/j.ijmachtools.2011.12.010

[20] Tajalli, S. a., Movahhedy, M. R., & Akbari, J. (2013). Chatter instability analysis of spinning micro-end mill with process damping effect via semi-discretization approach. Acta Mechanica, 225(3), 715–734. doi:10.1007/s00707-013-0981-4

[21] Bediz, B., Arda Gozen, B., Korkmaz, E., & Burak Ozdoganlar, O. (2014). Dynamics of ultra-high-speed (UHS) spindles used for micromachining. International Journal of Machine Tools and Manufacture, 87, 27–38. doi:10.1016/j.ijmachtools.2014.07.007

[22] Aran, V.(2011). Analysis on Micro Milling Dynamics and Stability (Master's thesis, Sabancı Üniversitesi, İstanbul, Turkey)

[23] Özşahin.O (2014). Analysis and modelling of machine tool dynamics and cutting stability during operation (Doctoral thesis, Middle East Technical University, Ankara, Turkey)

[24] J.D. Aristizabal-Ochoa, Timoshenko beam-column with generalized end conditions and nonclassical modes of vibration of shear beams, Journal of Engineering Mechanics 130 (2004) 1151–1159.

[25] E. Budak, Y.Altintas, Analytical prediction of chatter stability in milling – Part I: general formulation; Part II: application to common milling systems,, Trans, ASME: J. Dyn. Syst. Measur. Control 120 (1998) 22-36.

[26] Hendriks F.B.J.W.M. (2005). Chatter detection in high-speed milling, (April).